Alma Mater Studiorum · University of Bologna

School of Science
Department of Physics and Astronomy
Master Degree in Physics

Time resolution study of SiPMs as tracker elements for the ALICE 3 timing layer

Supervisor:
Prof. Gilda Scioli

Co-supervisor:
Dr. Francesca Carnesecchi

Submitted by:
Gianpiero Vignola

Academic Year 2020/2021

Abstract

Following the present ALICE, a next generation experiment at the LHC is under discussion (for LHC-Run5): ALICE 3. The idea is to have a superior tracking, vertexing, and timing all-silicon detector. For the Particle IDentification via Time Of Flight (PID-TOF), a detector capable of 20 ps time resolution positioned at 1 m from the interaction point is required. For this aim, a huge R&D phase on different technologies has just begun. Preliminary studies will be reported. In particular, the first time resolution study using SiPM detectors directly detecting Minimum Ionizing Particles will be discussed. The results will be also compared with laser measurements.

Contents

Introduction

The Silicon Photo-Multiplier (SiPM) detectors are widely used in the medical and technological industry as well as in nuclear and subnuclear physics as photon detectors. Their constructive properties and their operating principle guarantee an intrinsic high time resolution.

In this work, we will investigate the ability of SiPM to maintain excellent timing performances when used directly as Minimum Ionizing Particle (MIP) detectors. This technology, in fact, together with the Low Gain Avalanche Detectors (LGAD), is among the possible candidates as charged particle detectors for the TOF-layer of the future ALICE 3 experiment in which the entire tracking and timing system will consist of silicon detectors.

This work, and in general the studies of the research and development group for the ALICE 3 timing layer, represents the first-ever study of SiPMs used directly as MIP detectors. Some preliminary results of this innovative use of SiPMs will be presented here, providing interesting starting points for subsequent measurements. An in-depth 1054 nm laser characterization of studied SiPMs will be also presented and compared with CR studies.

In Chapter 1, after a brief introduction to silicon detectors and how charged particles and photons interact in them, some more in-depth considerations on timing properties will be discussed. The structure and operating principle of the SiPM will then be illustrated, followed by a brief analysis of another type of detector which is very performing in terms of time resolution, the LGAD. We will therefore move on to a brief review of possible applications of this type of detectors.

In Chapter 2, the ALICE 3 experiment, which is still in an embryonic design phase, will be illustrated with a description of the detector layout, a review of the main technologies involved, and a greater detail on the Timing layer, object of this work.

In Chapter 3, the core of this work will be presented. After a brief description of the devices followed by some preliminary studies, the setup, which involved three identical

Hamamatsu (HPK) SiPMs directly used as cosmic ray detectors, will be described. The results in terms of time resolution of this innovative approach will be compared with those obtained on the same detectors, using a pulsed laser of 1054 nm focused in a micrometric spot. Unexpected evidence concerning the crosstalk observed in the two setups will then be described. Finally, a brief, introductory analysis of the time resolution of some SiPM prototypes supplied by the Bruno Kessler Foundation (FBK) will be reported.

Chapter 1

Solid state detectors for timing applications

Solid-state detectors, mainly based on silicon and germanium technologies, are widely used in modern High Energy Physics (HEP) as excellent light and charged particles detectors. The inherent characteristics of the materials used, ensure applications such as precise measurements of time, position, and energy. In this chapter, after a brief presentation of the solid-state detector's operation, a comprehensive analysis of all the aspects that can spoil the time resolution will be presented. Subsequently, the characteristics of two types of detectors will be illustrated (SiPM and LGAD), followed by a brief review of possible applications of ultra-fast solid-state detectors.

1.1 Silicon detectors

A solid-state detector is essentially an ionization chamber, where the signal is produced by the movement of charge carriers. To make this possible, solid semiconductor materials are used, within group IV of the periodic table. Each atom in the crystal shares four valence electrons with four neighbor atoms. These materials behave like insulators at very low temperatures (near 0 K); at these temperatures, the electronic valence band structure is full. there are no electrons available for electrical conduction in the conduction energy band. At higher temperatures, due to thermal vibration, some of the bonds between the atoms of the lattice break, creating an electron-hole pair which is therefore available for the electrical conduction of the material. At the temperature of 300 K the density of electrons-holes for Silicon is about 10^{10} cm^{-3} which corresponds to an intrinsic resistivity of about 350 $K\Omega\, cm$ [1]. The energy gap between the valence band and the conduction band, under these conditions, is 1.115 eV.

Being very abundant in nature, and having been the subject of studies for years, Silicon, which can be operated at room temperatures, is mostly used in the electronics

industry and in HEP. From now on we will therefore talk about silicon detectors even if, for particular applications, other semiconductor crystals are preferable.

1.1.1 P-N junction and charge diffusion

In the main applications, a pure silicon crystal is never used but a doped structure is employed where some atoms are replaced with elements of the III, such as Borium (acceptors) or V group, such as Phosphorus (donors). Doing so, an excess of electrons or holes is introduced into the crystal, creating what is called P-type silicon or N-type silicon respectively. When P-type silicon is brought into contact with N-type silicon, the so-called P-N Junction is created. Due to the inhomogeneous distribution of the charge carriers, these will naturally diffuse from one region to the other. The flux $\vec{F}_p$ of the holes and $\vec{F}_n$ of the electrons is described by the equations:

$$\vec{F}_p = -D_p \, \vec{\nabla} p \tag{1.1}$$

$$\vec{F}_n = -D_n \, \vec{\nabla} n \tag{1.2}$$

With $\vec{\nabla} n$ and $\vec{\nabla} p$ the graients of electrons and holes denities, D_n and D_p diffusion constants $[cm^2/s]$, related to the temperature T by the Einstein relation:

$$D_i = (\frac{kT}{q})\mu_i \tag{1.3}$$

Here μ_i is the mobility of the charge carriers $[cm^2/Vs]$, $k = 8,617^{-5} \, eVK^{-1}$ the Boltzmann constant and $q = 1,602 \times 10^{-19} \, C$ the Elementary Charge. μ_i depends on doping and temperature, for intrinsic silicon at 300 K the mobilities are respectively $\mu_n \sim 1350$ cm^2/Vs and $\mu_p \sim 450$ cm^2/Vs. The diffusion proceeds until the equilibrium condition is reached. The remaining ions create a space charge and an electric field that stops the diffusion creating an intermediate region in the P-N junction free from charge carriers: The depletion region Figure 1.1.

1.1.2 Electric field and charge drift

The movement of the charge carriers in an electric field E, usually called drift, can be described by the relations:

$$\vec{v_p} = (\frac{q \, \tau_c}{m_p})\vec{E} = \mu_p \, \vec{E} \tag{1.4}$$

$$\vec{v_n} = (\frac{q \, \tau_c}{m_n})\vec{E} = \mu_n \, \vec{E} \tag{1.5}$$

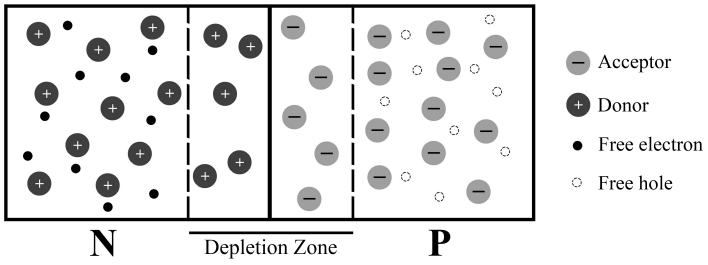

Figure 1.1: P-N junction

It is possible to note that the drift velocity $\vec{v_p}$ and $\vec{v_n}$, are directly proportional to the mobility μ_n of the electrons and μ_p of the holes. In the derivation of these formulas, it is assumed that the charge carriers with charge $\pm q$ and mass m_i move in the lattice accelerated by the electric field losing energy through scattering in the imperfections. τ_c is the mean time between successive collisions. For large $\vec{E}$, τ_c decreases until the drift velocity is saturated. Considering the PN junction described in the previous paragraph, the application of an external Voltage can expand or decrease the size of the depletion region. A forward bias voltage V increases the natural diffusion of charge carriers by reducing the depletion zone. A reverse bias voltage, instead, increases the size of the depletion zone, Figure 1.2.

Combining the contributions of diffusion and drift of electrons and holes, it is possible to derive the total current density of the charge carriers:

$$\vec{J_p} = q\mu_p p\vec{E} - qD_p\vec{\nabla}p \tag{1.6}$$

$$\vec{J_n} = -q\mu_n n\vec{E} - qD_n\vec{\nabla}n \tag{1.7}$$

It should be noted that this relationship is valid with electric fields $\vec{E}$ that are not too intense and in the absence of external magnetic fields that can curve the trajectory of the charge carriers. In extremely-high $\vec{E}$ conditions, the energy acquired by the individual charge carriers can be enough to produce a new electron-hole pair. This can trigger an avalanche process and create an electrical breakdown of the devices. Avalanche processes of this type are exploited, for example, in SiPMs that work above the breakdown voltage, or in controlled range in LGAD technologies (more details in sections 1.4 and 1.5).

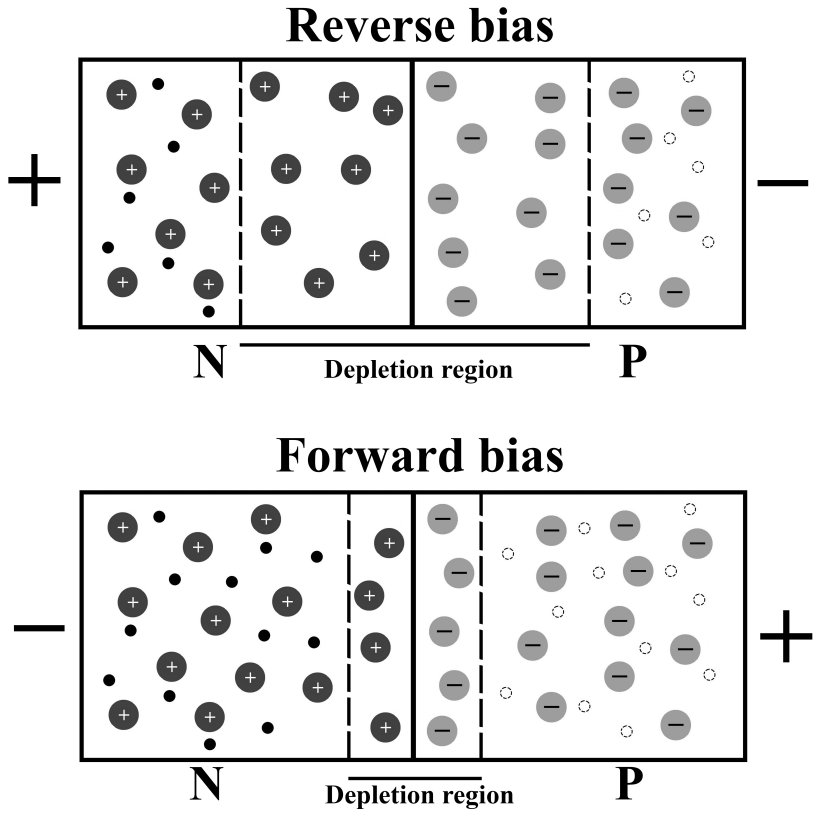

Figure 1.2: P-N junction with different polarization

1.2 Passage of particles through silicon detectors

The operating principle of a silicon detector (p-on-n type) is illustrated in Figure 1.3. The standard structure of a silicon detector consists of a P-N junction with heavily doped p^+ and n^+ electrodes. These are separated by a lightly doped n^- type bulk. the heavily doped n^+ silicon, in reverse biasing conditions, is directly connected to the positive electrode where the negative charges are collected. On the other hand, the p^+ silicon is connected with the negative electrode in which the holes are collected. A sufficient reverse bias is applied to create a depletion region that is large enough. This will be almost coincident with the active region of the detector. Here charged particles or photons will be able to interact with the detector structure, creating electron-hole pairs which, being the only mobile charges in this region, will produce a signal (or rather will induce a current that can be measured). There is signal until all charge carriers have reached their respective collection electrodes.

In this section the physics of particle-silicon interactions will be briefly summarized, distinguishing the cases of heavy charged particles, electrons, and photons.

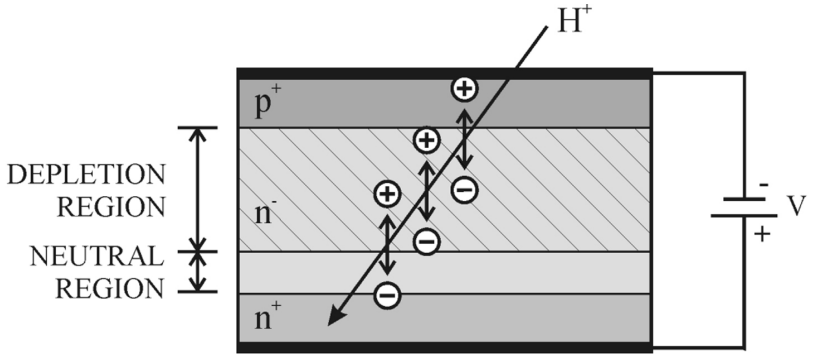

Figure 1.3: The operating principle of a silicon detector (p-on-n type)[2]

1.2.1 Hadron Charged Particles

Hadron charged particles, entering into a material with velocity $v = \beta c$, interact with lattice atoms causing, in most cases, ionization through electron stripping. The energy transferred to an electron in a single collision is of the order of 100 eV (in rare cases even > 10 KeV) well above the energy needed to create an electron-hole pair in the Silicon. It must also be considered that the depletion region crossed by a charged particle in a detector has a certain thickness so that more interactions will occur along the path, producing several electron-hole pairs. The charged particles produced in the primary interactions can, if sufficiently energetic, further interact in the material creating the so-called secondary ionization. The number n_{tot} of electron-hole pairs (primary and secondary) produced by the passage of a charged particle through the silicon is stochastic. As a first approximation it can be calculated as:

$$n_{tot} = \frac{\Delta E}{W} \tag{1.8}$$

where ΔE is the energy released by the incident particle into the silicon and W the average energy required to form an electron-hole pair, about 3.6 eV in the silicon at room temperature. The energy ΔE released can be better expressed as the product of the thickness dx of the crossed silicon multiplied by the stopping power S:

$$\Delta E = dx\, S \tag{1.9}$$

S is better known as the Bethe-Bloch formula and expresses the mean rate of the energy loss in a material with the atomic number Z and mass A by an incident particle with charge z and relativistic parameter β:

$$S = -\frac{dE}{dx} = K\,\frac{Z}{A}\,\frac{z^2}{\beta^2}\,(ln(\frac{2m_e\gamma^2v^2W_{max}}{I^2}) - 2\beta^2 - \delta - 2\frac{C}{Z}) \tag{1.10}$$

Here K is a constant 0.1535 $[MeV\ cm^2/g]$, m_e the mass of the electron, relativistic $\gamma = 1/\sqrt{1-\beta^2}$ and v velocity of the incident particle, W_{max} the maximum kinetic energy transferred to an electron in a single collision , I the average ionization potential of the material and δ and C respectively density and shell correction factors. It provides a good description of the average energy released by heavy relativistic charged particles in the region $0.1 < \beta\gamma < 1000$ for medium Z materials with a few percent accuracies. For lower $\beta\gamma$ the speed of the projectile becomes comparable with that of the electron and low energy corrections must be considered. Above this range, on the other hand, radiative effects dominate. An example of the stopping power of muons in copper is shown in Figure 1.4.

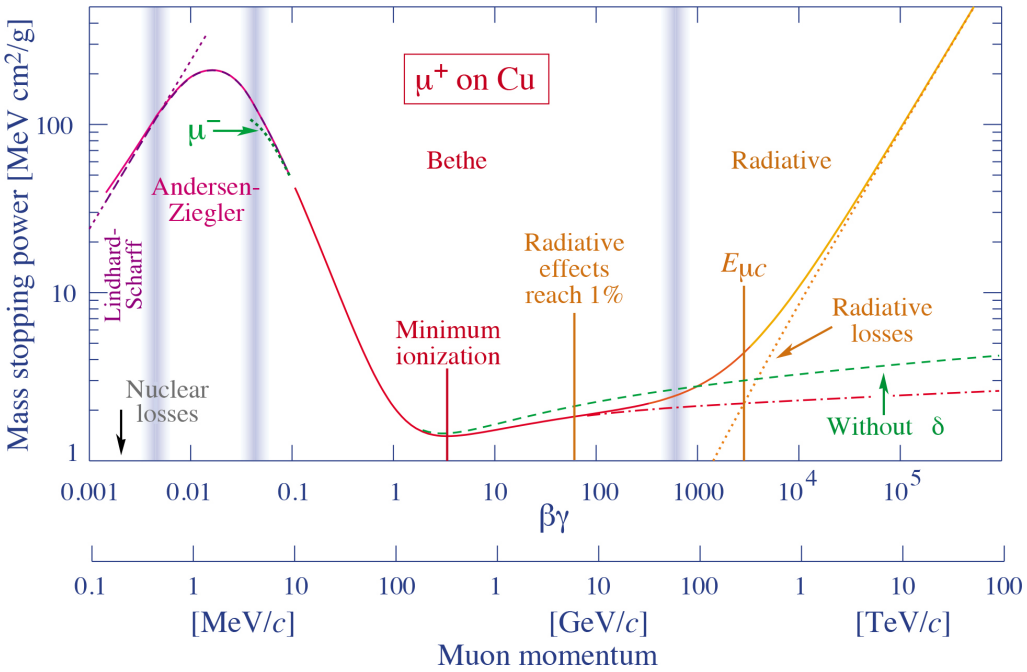

Figure 1.4: Stopping power of muon in copper as function of the $\beta\gamma$ and muon momentum.[3]

1.2.2 Electrons and Positrons

The stopping power of electrons and positrons S_e differs greatly from that of heavy charged particles. In this case, the projectile and target have the same mass so that the energy lost by the projectile in a single collision is significantly higher than the case described in the previous paragraph. The Bethe-Bloch formula must be modified, taking into account the indistinguishability of the particles:

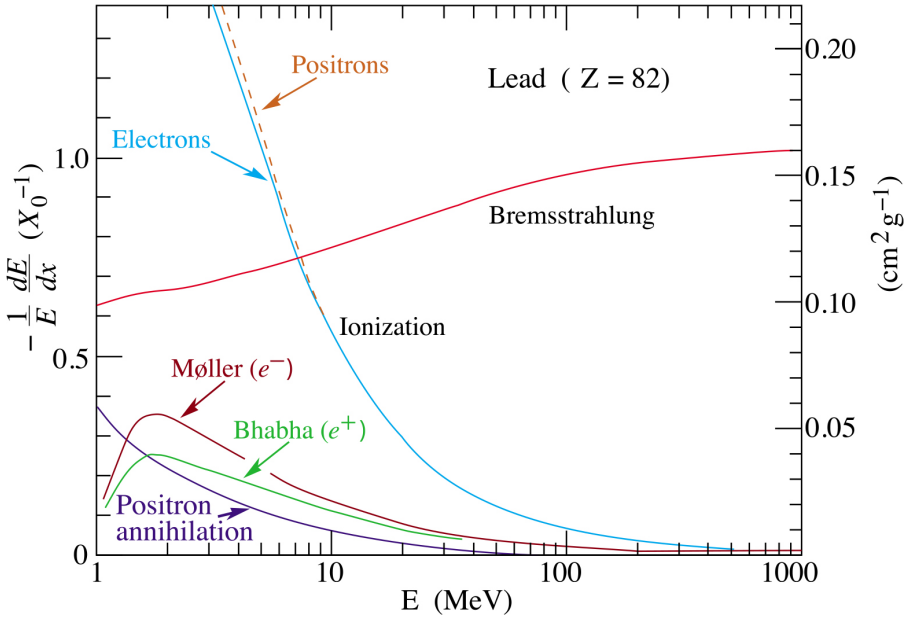

Figure 1.5: Stopping power of positron/electron in lead [3]

$$S_e = -\frac{dE}{dx}_{ion} = k\,\frac{Z}{A}\,\frac{1}{\beta^2}\,(ln(\frac{m_e\gamma^2 v^2 T}{2I^2}) + F(\gamma)) \tag{1.11}$$

Where T is the kinetic energy of the electron and $F(\gamma)$ are corrections. Moreover, due to their small mass, electrons and positrons, interacting with the nuclear magnetic field of the medium, lose energy via Bremsstrahlung by emitting photons. The energy lost through this process is found to be proportional to the energy E of the projectile and inversely proportional to the square of its mass m:

$$-\frac{dE}{dx}_{bremss} = \frac{E}{X_0} \propto \frac{E}{m^2} \tag{1.12}$$

In this context, it is useful to define the radiation length X_0, which is the average distance in which an electron, passing through a certain material, reduces its energy to a factor $1/e$ of the initial energy through Bremsstrahlung emission. X_0 is a constant of the material, for silicon it is $X_0 = 21.82\ g/cm^2$.
Adding the two contributions, the energy lost by electrons and positrons in a medium is therefore:

$$\frac{dE}{dx} = \frac{dE}{dx}_{ion} + \frac{dE}{dx}_{bremss} \tag{1.13}$$

An example concerning the $\frac{dE}{dx}$ in lead is shown in Figure 1.5. It is interesting to note, that the second radiative term becomes dominant above few tens of MeV. In particular, in solids, radiative energy losses and energy lost by ionization are equal when the projectile energy reaches the critical value E_c:

$$E_c = \frac{610\,MeV}{Z + 1.24} \tag{1.14}$$

In pure silicon (Z = 14) this condition occurs at E_c of about 40 MeV.

1.2.3 Photons

As known, photons have no charge and are massless. Interacting with matter, they produce one or more charged particles that can create electron-hole pairs in the silicon. Depending on the energy of the incident photon, it can interact in at least 3 ways: photoelectric effect, Compton scattering, and pair production :

$$\gamma + atom \rightarrow atom^+ + e^-,\ Photoelectric\,Effect \tag{1.15}$$

$$\gamma + e^- \rightarrow \gamma + e^-,\ Compton\,scattering \tag{1.16}$$

$$\gamma + nucleus \rightarrow nucleus + e^- + e^+,\ Pair\,production \tag{1.17}$$

Figure 1.6 shows an example of the different cross sections as a function of energy for carbon and lead.

It is important to note that, unlike the charged particles, the detection of a photon is a destructive process: after its interaction, the incident photon will no longer be available for subsequent measurements (partially true also for electrons and positrons). The intensity I of a beam of photons with initial intensity I_0 as a function of the thickness of the material traversed x can therefore be expressed as:

$$\frac{I}{I_0} = e^{-\alpha x} \tag{1.18}$$

Where α, called absorption coefficient, is a typical constant of the material. Its analytical expression is the following:

$$\alpha = \frac{\sigma N_A \rho}{A} = \frac{1}{\lambda} \tag{1.19}$$

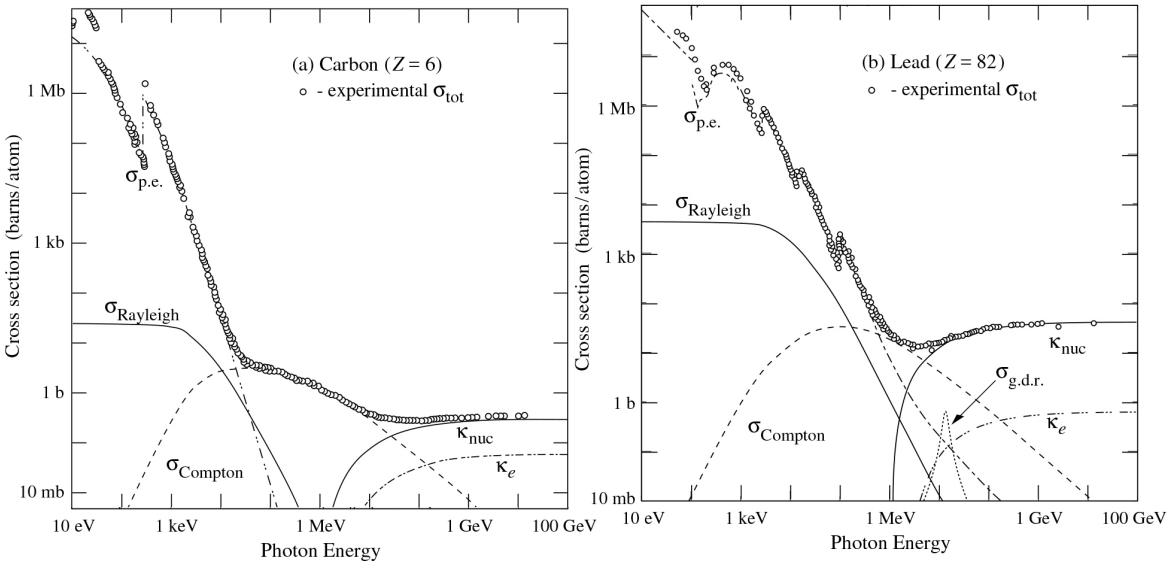

Figure 1.6: Photon cross sections as a function of energy in carbon and lead [3]

Where σ is the total cross section, N_A the Avogadro number, ρ and A density and mass number of the material. λ is the mean free path that is the average distance traveled by the photon before interacting. Focusing on photons with wavelengths in the range 200-1100 nm in Figure 1.7 an example of average absorption depth in standard silicon at a temperature of 300 K is reported. Each silicon detector has its active area (depleted region) at different depths. Selecting opportunely the wavelength, a beam of photons with appropriate focus and appropriately tuned, can, in a first approximation, simulate a charged particle that passes through a silicon detector creating, along the track, the same number of electron-hole pairs in the active region of the detector. It is important to underline, however, that the physical mechanisms of the two interactions are completely different.

1.3 Silicon for timing

In the section 1.2 the operating principle of a standard silicon detector has been briefly illustrated. In this section, we will analyse the construction and operating details characteristic of silicon detectors optimized for timing measurements.

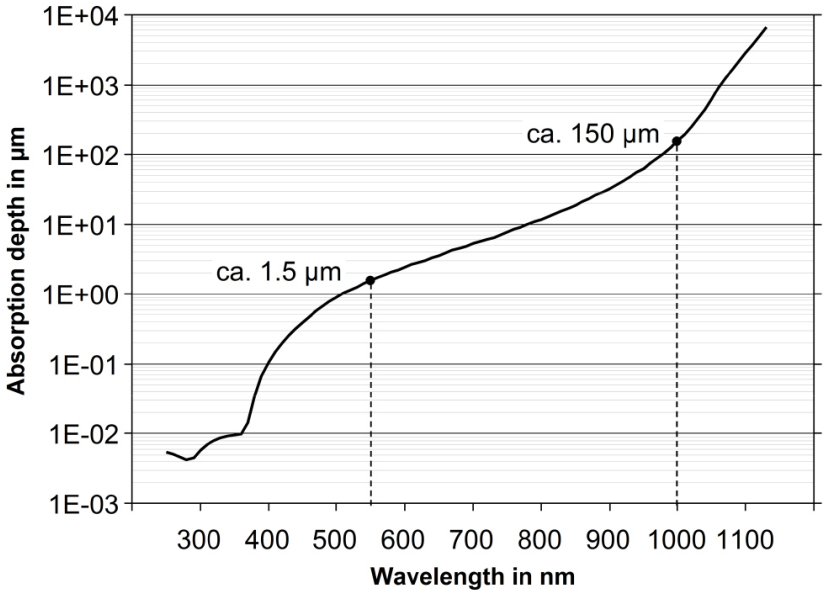

Figure 1.7: Absorption depth of silicon at 300 K as a function of the wavelength [4]

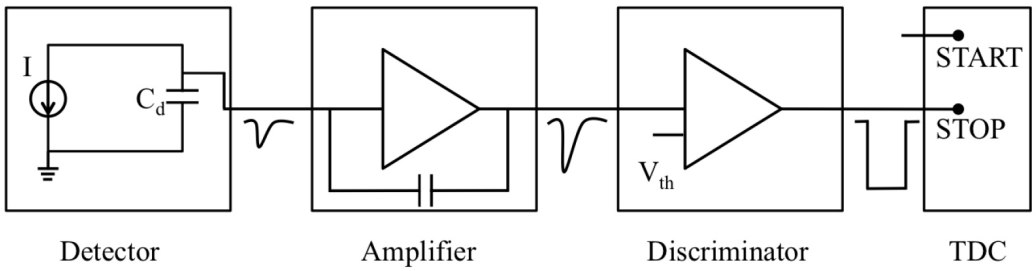

Figure 1.8: Time-measurement system chain [5]

1.3.1 Time resolution

A typical time measurement system can be represented as in Figure 1.8. The silicon detector can be schematized as a current generator in parallel with a capacitance. The current signal is first amplified and then usually discriminated with a threshold system. A Time to Digital Converter (TDC) is then used to measure the time interval between the trigger (which starts the TDC, produced by another detector or coming from an external source related to the primary event) and threshold crossing. In the measured time resolution of a silicon detector, it is possible to recognize at least 5 contributions [6] added quadratically:

$$\sigma_t^2 = \sigma_{TS}^2 + \sigma_{Landau}^2 + \sigma_{Dist.}^2 + \sigma_{Jitter}^2 + \sigma_{TDC}^2 \tag{1.20}$$

- The Time slewing term σ_{TS}^2 and the Landau term σ_{Landau}^2 are due to the nature of the energy deposition process by the charged projectile. Each signal is different and the energy released changes. Depending on the amplitude of the signal, this can exceed before or after the chosen threshold. This effect, called time slewing, can be easily corrected by analyzing the maximum amplitude of the signal or the charge deposited. If the signal is assumed to be linear, with rising time t_r and amplitude S, the delay t_d due to the time slewing is written:

$$t_S \propto \frac{t_r\, V_0}{S} \tag{1.21}$$

  with V_0 threshold voltage. The associated error σ_{TS} is therefore given by the RMS of the t_d:

$$\sigma_{TW} = [t_d]_{RMS} \tag{1.22}$$

  The Landau term, on the other hand, is linked to the variability with which a MIP interacts in the silicon: The energy deposited by an incoming particle with a given energy is in fact distributed according to the Landau distribution.

- The distortion term $\sigma_{Dist.}^2$ is strongly correlated with the uniformity of the Electric field which causes changes in the shape of the signal from event to event.

- The jitter term σ_{Jitter}^2 is due to the presence of electronic and detector noise. When the signal is rising, the threshold comparator can trigger early or late depending on how the noise acts at that point. σ_{Jitter} is therefore directly proportional to the RMS of the noise σ_N and inversely proportional to the slope of the signal near the threshold value:

$$\sigma_{Jitter} = \frac{\sigma_N}{dV/dt} \tag{1.23}$$

- The term related to the TDC, σ_{TDC}, is a constant that can be expressed as:

$$\sigma_{TDC} = \frac{TDC_{bin}}{\sqrt{12}} \tag{1.24}$$

where TDC_{bin} is the width in time of the least significant bit of the TDC used.

The first 3 terms are related to the particle-detector interaction and the detector construction parameters, henceforth we will refer to these contributions as intrinsic resolution σ_{intr}, the equation 1.20 then becomes:

$$\sigma_t^2 = \sigma_{intr}^2 + \sigma_{Jitter}^2 + \sigma_{TDC}^2 \tag{1.25}$$

1.3.2 Thickness of detectors

A large signal, and therefore a large signal to noise ratio, is one of the main characteristics required to improve the time resolution. This can suggest that increasing the thickness of the active area and thus the number of charges deposited by the incident particle is the best solution for timing purposes. In reality, Ramo-Shockley's theorem [6] shows that the maximum current I_{max} in a silicon detector is independent of the thickness d of the detector itself:

$$I_{max} \propto nqv_{sat}\frac{1}{d} = Ndqv_{sat}\frac{1}{d} = Nqv_{sat} \tag{1.26}$$

Here q represents the elementary charge, v_{sat} stands for the saturation velocity of the charge carriers (under conditions of large electric fields) and $N = n/d$ represents the number of pairs produced per μm. A typical value for the I_{max} produced by a MIP in a silicon detector is $I_{max} \sim 1.5\ \mu A$ [6]. Therefore, increasing the thickness of the detector is not the optimal solution, on the contrary, considering the limit velocity of the charge carriers ($\sim 10^7\ cm/s$) a deep detector corresponds to a longer collection time.

1.3.3 Gain

As previously mentioned, the best time resolutions are obtained when the electron and hole velocity is saturated and this is verified for electric fields $E > 10^4\ V/cm$. Under these conditions, the electrons travel 1 μm in 15 ps while the holes travel the same space in 30 ps. A typical silicon detector of 300 um thickness is therefore covered in 10 ns by electrons and 25 ns by holes (collection time). Another very important factor is that the electric field must be as uniform as possible in order to have a uniform charge collection. The simplest way to obtain a uniform electric field inside the sensor is to make detectors

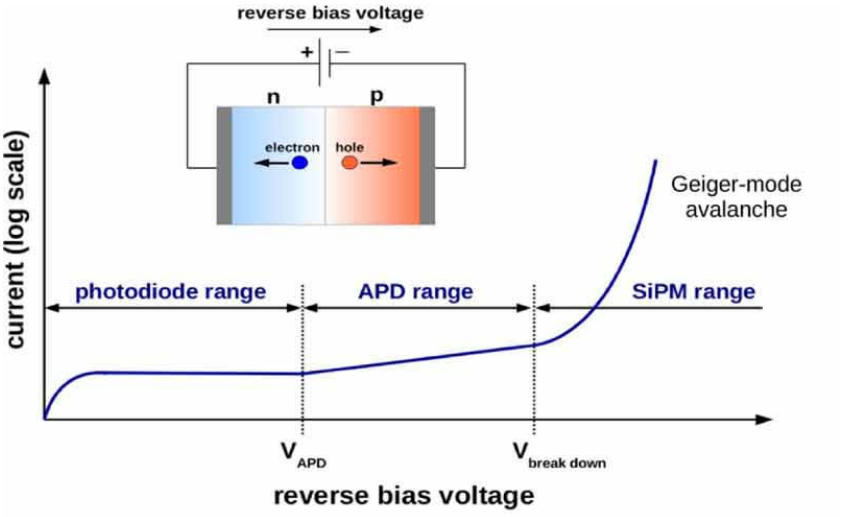

Figure 1.9: Operation regimes of solid state detectors [7]

with geometry as close as possible to a flat capacitor with the area of the single cell >> of sensor thickness.

Even if the above conditions are met, standard silicon detectors have limited time resolutions. Increasing the amplitude of the signal, and therefore the slew rate, is what improves the performance. Taking advantage of avalanche multiplication processes, such as in gas detectors, can be a solution. In the detectors discussed here (LGAD and SiPM) this is done in limited, under control regions of the sensor, where the electric fields are so high as to allow the primary electron-hole pairs to create secondary pairs. This condition occurs for very high electric fields. In this region, the multiplication is still in linear regime (Proportional Avalanche Photo-Diode mode, gain 50-500), further increasing the electric fields we enter into Geiger-mode: electrons and holes produce avalanche processes in an uncontrolled way and the detector goes into breakdown (GM-APD Gain $\sim 10^4$): the current increases exponentially increasing the reverse bias Figure 1.9.

1.4 SiPM, Silicon Photo-Multiplier

The silicon detector on which this study primarily focuses is the analog Silicon Photo-Multiplier (SiPM): an array of Single-Photon Avalanche Diodes (SPADs) independent and read in parallel. The detector, developed as the technological evolution of the classic photomultiplier, has reached very high performance in recent years in terms of single-photon sensitivity, with good intrinsic time resolutions. This type of detector is nowadays widely used in the technological and medical industry but also in the field of HEP.

1.4.1 The Avalanche Diode and the SPAD

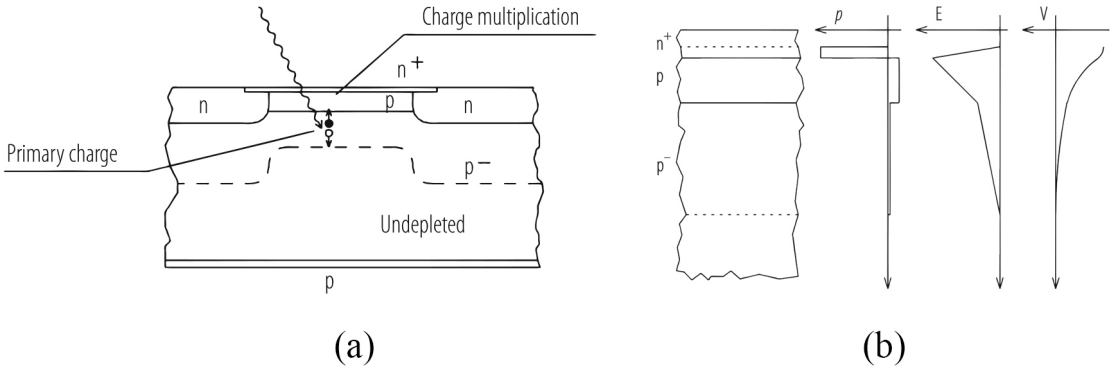

Figure 1.10: Avalanche Diode built on p-type silicon (a), amplification region with charge density, electric field and potential profile (b) [1]

As previously mentioned, some silicon detectors, have areas with a very high electric field where the avalanche multiplication of the charges takes place. One example is the Avalanche Diode AD. In Figure 1.10(a) it is possible to see an example of AD built on p-type silicon.The structure consists of a thin highly doped n-type layer on the surface(n^+ Figure 1.10(a)), followed by a moderately doped p-type layer (p in Figure 1.10(a)). The thick substrate p^- is completely depleted in the upper part, this region is the drift zone. In Figure 1.10(b) it is possible to see a detail of the amplification region where the charge densities ρ (charge density, doping), the electric field E and the potential V are reported. It is possible to note that the region with the highest electric field is the one corresponding to the $n^+ - p$ junction: amplification zone.

In this type of junction, the electrons produced below the region with high electric field drift towards n^+ in high electric field conditions and acquire enough energy to create additional electron-hole pairs. Similarly, the holes produced above the high E region will drift downward and, if sufficiently accelerated, may start charge multiplication.

The avalanche process increase with the applied voltage. The avalanche diode, as previously mentioned, can work in linear mode (medium electric fields) or Geiger-mode (higher electric field). The avalanche continues until stopped by statistical fluctuations or until a sufficient decrease of the electric field (applied voltage) happens. When the detector works in Geiger-mode it is not possible to have a signal proportional to the charge released by the incident particle however, the detection of a single photon becomes possible.

The SPAD is a particular type of GM-APD (Geiger-mode Avalanche Photo-Diode).

A realistic structure of the SPADs, used in the SiPMs, is shown in Figure 1.11. The picture schematizes the two types of SPAD, n-on-p and p-on-n.

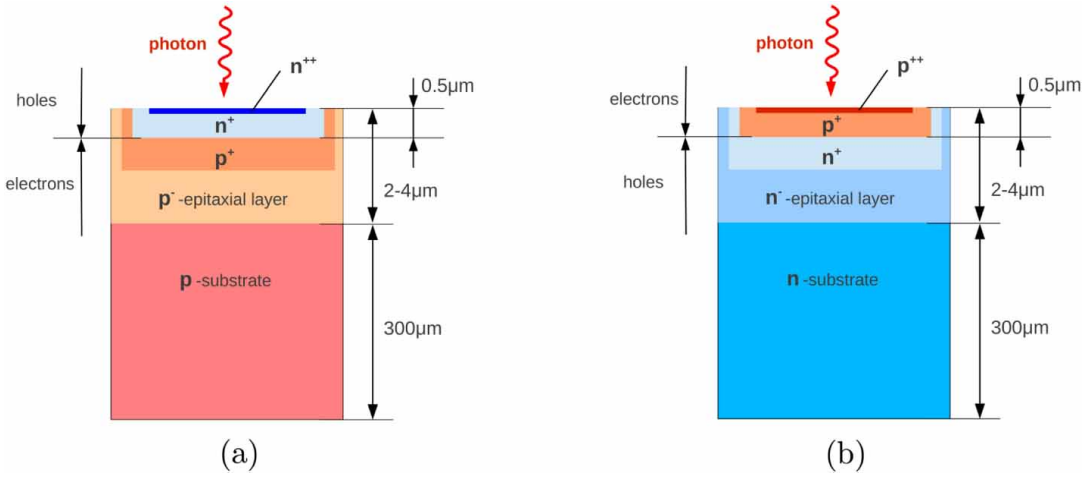

Figure 1.11: The n-on-p SPAD structure (a), the p-on-n SPAD structure (b) [7]

1.4.2 SiPM structure and working principles

An analog SiPM is a matrix composed by 100-10000 SPADs with typical dimensions between 10 μm^2 and 100 μm^2. They are read in parallel and each one is connected with a quenching resistor R_q which is used to interrupt the process of uncontrolled multiplication when a single SPAD produces an avalanche Figure 1.12.

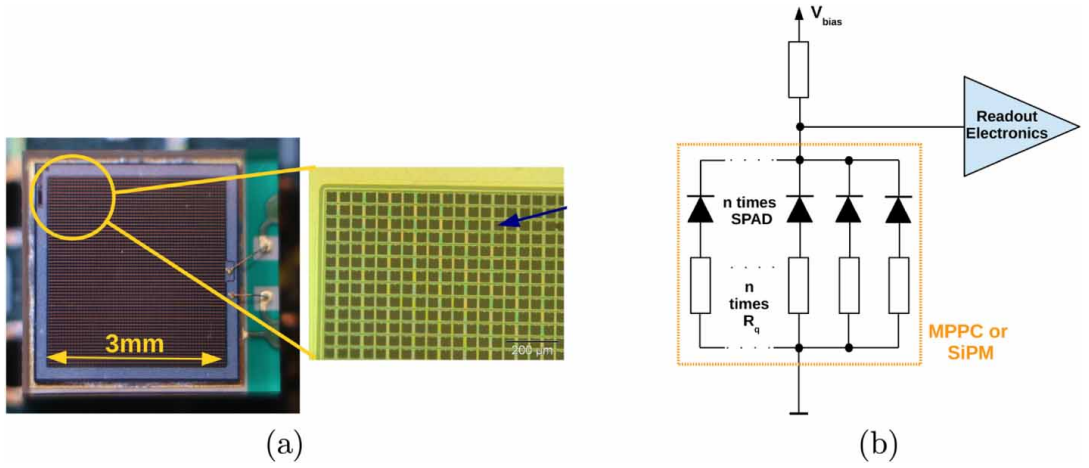

Figure 1.12: An analog SiPM structure [7]

When one or more SPADs enter Geiger-mode, approximately 10^4-10^6 elementary

charges for each triggered SPAD are produced. Being connected in parallel, the signal produced will be proportional to the number of triggered SPADs. On the other hand, it is not possible to distinguish the cases in which a single SPAD is hit, for example, by several photons; the signal produced will be the same, and therefore indistinguishable from that initiated by a single photon.

The SiPM single pixel (SPAD) equivalent circuit is depicted in Figure 1.13. The

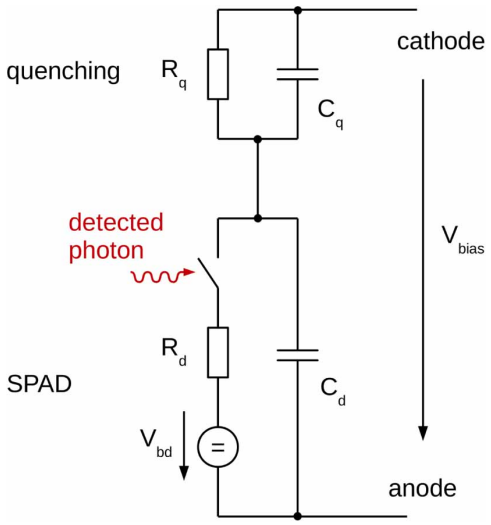

Figure 1.13: SPAD equivalent circuit [7]

SPAD can be seen as a connection in parallel between the whole resistance of the diode R_d and its internal capacitance C_d (sum of the area capacitance of the SPAD and any perimeter or parasitic capacitances). The series quenching circuit is composed of the quenching resistor R_q in parallel with a parasitic capacitance C_q. In the quiescent state, the voltage on C_d is the applied voltage V_{bias}. A signal induced by a photon (or by a noise event) can, in this model, be seen as the closure of the switch in the figure. This causes an exponential voltage drop in the node between C_q and C_d and capacitor C_d starts to discharge. At the same time, the capacitor C_q begins charging through R_d. The capacitances involved in the charging process is $C_q + C_d$ and the voltage discharge time constant τ_d is:

$$\tau_d = R_d(C_q + C_d) \tag{1.27}$$

Note that the influence of R_q has been neglected (R_q generally very large). The V_{bd} used in the model, represents the voltage of the breakdown over which the avalanche process starts in the SPAD, which is the maximum voltage drop at the internal node. Starting from this it is possible to define the overvoltage V_{ov} as:

$$V_{ov} = V_{bias} - V_{bd} \tag{1.28}$$

The discharge of C_d and recharges of C_q end when the current through R_d reaches the value I_d which is approximately:

$$I_d \simeq \frac{V_{ov}}{R_q + R_d} \sim \frac{V_{ov}}{R_q} \tag{1.29}$$

The avalanche at this point is "quenched", the cell returns to its initial conditions with a recharge time constant:

$$\tau_r = R_q(C_q + C_d) \tag{1.30}$$

The gain G of the SPAD can be expressed as the ratio between the total charge involved in the avalanche and elemental charge q:

$$Gain = \frac{avalanche\_charge}{q} = \frac{V_{ov}(C_q + C_d)}{q} \tag{1.31}$$

1.4.3 Primary and secondary noise

In the SiPM detectors, there are two sources of noise: primary and correlated (or secondary). The main primary source of noise is represented by the Dark Count Rate (DCR) i.e. noise events due to a thermally generated electron-hole pair that trigger an avalanche generating a false signal (Figure 1.14(a)). This trend is strongly dependent on the temperature it decreases by a factor of 2 every 10 K drop in temperature [7]. The DCR can be improved through specific production processes and material purity. two examples of correlated noise are Afterpulsing and Crosstalk. Afterpulsing consists of events following the main event (signal or Dark Count event) due to the progressive release of charges trapped in the high E region during the avalanche, APdiff in Figure 1.15 (example of dark count of signal with afterpulse in Figure 1.14(b)). This generally involves the same cell in which the primary event occurred. The probability of afterpulse depends on the number of traps, release time constant, and recharge time equation 1.30. The afterpulse can be reduced by selecting the material, for example by using a low-lifetime substrate.

1.4.4 Crosstalk

One type of correlated noise that in the context of this work deserves a separate discussion is the crosstalk in SPADs neighbours within the SiPM-array. In an avalanche up to

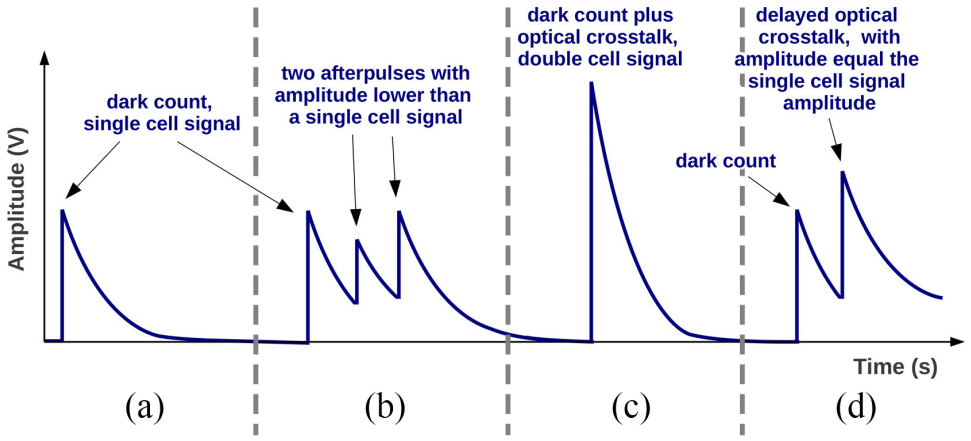

Figure 1.14: Analog SiPM output signal of different kinds of noise, adapted from[8]

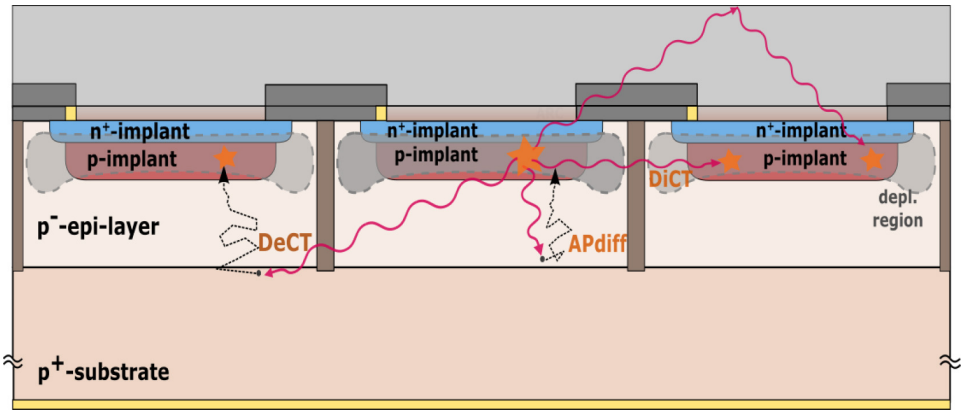

Figure 1.15: Analog SiPM crosssection with the different type of correlated noise [8]

3×10^{-5} photons for charge carriers can be produced [9]. The isotropically emitted photons can reach neighbouring cells, producing a signal in these SPADs (this effect is generally reduced with the introduction of trenches between adjacent cells). As a result, more SPADs are triggered simultaneously (considering the proximity between the cells and the velocity of photons in the material) even if a single incident photon hits a single SPAD. This type of crosstalk is called direct optical crosstalk or prompt optical crosstalk Figure 1.15 DiCT (example of dark count signal with Direct CT in Figure 1.14(c)). Note that the figure also shows the case in which a photon produced in an avalanche reaches an adjacent cell through internal reflections in the protective layer of the SiPM or possibly reflections due to the presence of an object coupled with the SiPM. Another type of crosstalk called delayed optical crosstalk, shown as DeCT in the Figure 1.15, is due to the creation of an electron-hole pair in the bulk, which subsequently, by diffusing, reaches the active region producing an avalanche (delays from some ns to μs) (example of dark

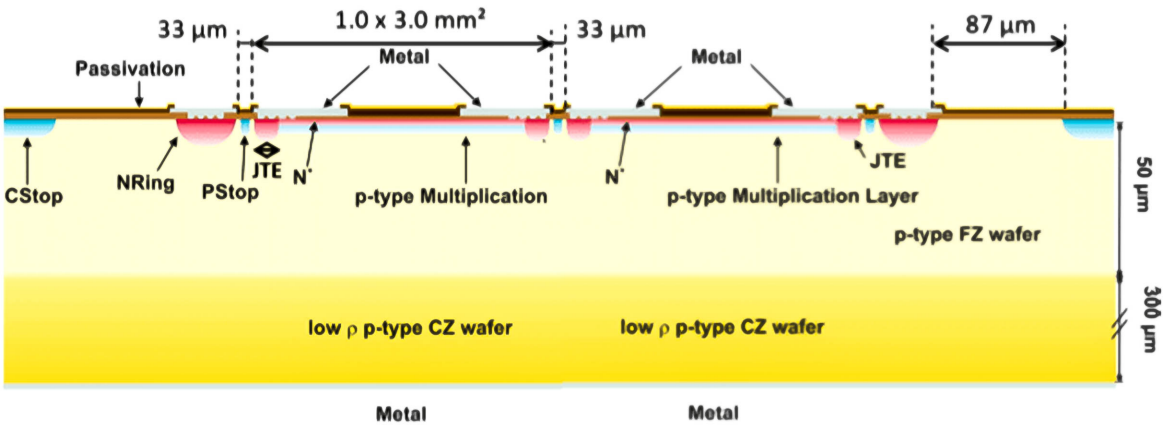

Figure 1.16: Typical multi-pixels LGAD structure. In the figure: the multiplication layer, the JTE and the p-stop to isolate the neighbouring pads. adapted from [10]

count signal with delayed CT in Figure 1.14(d)).

1.5 LGAD, Low Gain Avalanche Detectors

The SiPMs described in the previous chapter and, in general, silicon detectors with very high gains, are widely used, for example, as single-photon detectors as they are able to create a signal starting from a single primary electron-hole pair. In the field of high energy physics with MIP (Minimum Ionizing Particles), however, where the number of pairs created by the passage of a particle is of the order of 73 $pairs/\mu m$ [6], other types of silicon detectors with much lower gain may be a better option. This is the case of the Low Gain Avalanche Detectors, also called Ultra-Fast Silicon Detectors (UFSD), with particular emphasis on their very high capacity in terms of time resolution.

1.5.1 LGAD structure

The typical structure of an LGAD is shown in Figure 1.16. This follows the general structure of an AD already described, but here the active bulk is much thicker (25-300 μm) and the single-pixel is generally larger (some mm). In the example shown (n-in-p silicon detector) it is possible to see the highly doped gain layer (p+ doping of the order of 10^{16} $atoms/cm^3$) inserted below n^+ surface silicon. This creates a very intense electric field region (E order of 300 kV/cm) in the junction area between n^+ and p^+ few micrometers thick, which is the multiplication area. The remaining part of the detector is instead called "Drift region" (p-type FZ wafer in Figure 1.16). In this zone, there is no multiplication of charge as the electric field is too low (order of 30 KV/cm). Often

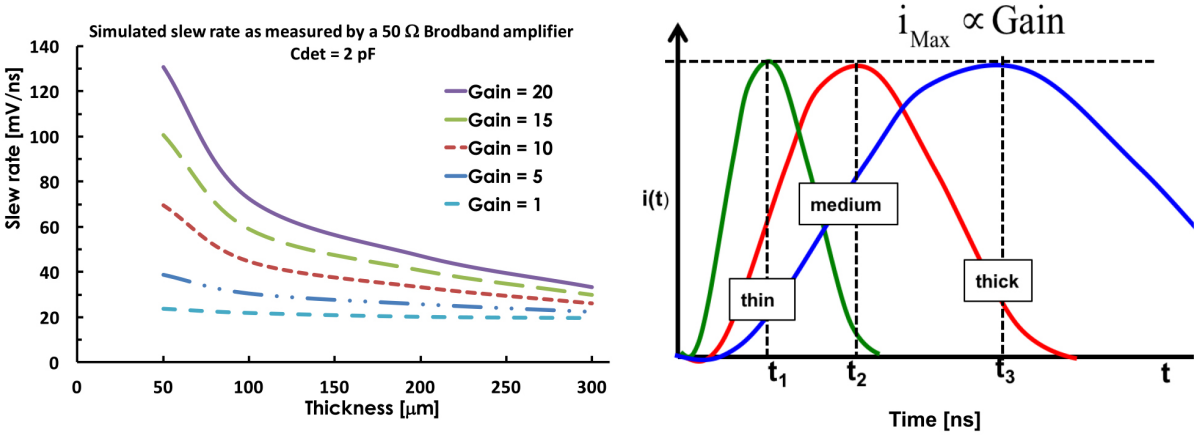

Figure 1.17: Signal slew rate as a function of sensor thickness for different values of gain (left). Signals from sensors with equal gain and different thicknesses (right) [6]

one or more Junction Termination Extensions (JTE) and p-stop are inserted to ensure uniformity in the electric field, as mentioned, very important for the time resolution and to isolate the neighbouring pads.

1.5.2 Peculiar properties

The main feature of an LGAD is its low gain. High gain sensors such as the SPADs discussed above, suffer from problems related to noise [6]. A MIP produces many primary e-h pairs in the sensor. Therefore, the idea is to minimize the gain sufficiently to have an accurate measurement of the crossing time of the incident particle. Another very important parameter is the thickness of the detector. A thin detector corresponds to a shorter time of drift so that the maximum of current is reached in a shorter time (high slew-rate) and the time performance improves. However, a too-thin detector corresponds to a large sensor capacity. In order to improve interfacing with the amplification's electronics, this capacity must have appropriate values to ensure an accurate measurement. A good trade-off between thickness and capacity (also related to the sensor area) is therefore necessary.

For an LGAD detector, or generally for all silicon detectors with gain, given the thickness d of the detector and the gain G, it is possible to determine the maximal current di_{gain} generated from new pairs dN_{gain} created in the multiplication area:

$$di_{gain} = dN_{gain} q v \frac{1}{d} \propto \frac{G}{d} dt \tag{1.32}$$

It is so possible to derive the important result:

$$\frac{di_{gain}}{dt} \sim \frac{dV}{dt} \propto \frac{G}{d} \tag{1.33}$$

Which suggests thin detectors as the best configuration from the time resolution point of view. It is also possible to derive the maximum current for an LGAD and verify that this is proportional to the gain [6]. In Figure 1.17, we can see the results of slew-rate simulations as a function of the thickness for different gains (left) and examples of signals for different thicknesses of the detector (right). It is possible to notice how the slew rate, and therefore the speed with which the signal reaches the maximum current, increases rapidly by decreasing the thickness of the LGAD or increasing the gain. Thicknesses of the order of 50 μm (or less) and gains of the order of 20-30 represent a good compromise for timing applications and allow to reach time resolutions of a few tens of ps.

1.6 Possible applications of extremely fast silicon detectors

1.6.1 Time Of Flight PID

When the particles produced in a collision have a momentum of some GeV/c, the best PID method is the TOF technique where the velocity of the particles is directly measured. A TOF detector measures the crossing time t of a particle at a distance L (known from tracking) from the Interaction Point IP. Knowing the momentum (using a magnetic spectrometer) of the particle, it is possible to obtain its mass m, and then identify it using the relation [11]:

$$m = p\sqrt{\frac{c^2\,t^2}{L^2} - 1} \tag{1.34}$$

where m and p are measured in eV. Starting from the previous relation it is possible to obtain the resolution in the mass measurement:

$$\left(\frac{dm}{m}\right)^2 = \left(\frac{dp}{p}\right)^2 + \left(\gamma^2\,\frac{dt}{t}\right)^2 + \left(\gamma^2\,\frac{dL}{L}\right)^2 \tag{1.35}$$

where in most cases $\gamma >> 1$. Assuming that the measurement of p is precise ($\frac{dp}{p} = 1\%$) and considering a negligible error in the measurement of L, the dominant factor in the mass resolution is the time resolution dt of the used detector. A better time resolution of the timing layer corresponds to a smaller error in the mass of the particle measured when the TOF method is used.

To determine the particle identification efficiency of a TOF detector, it is useful to look at the difference in the Time Of Flight of two different particles with the same

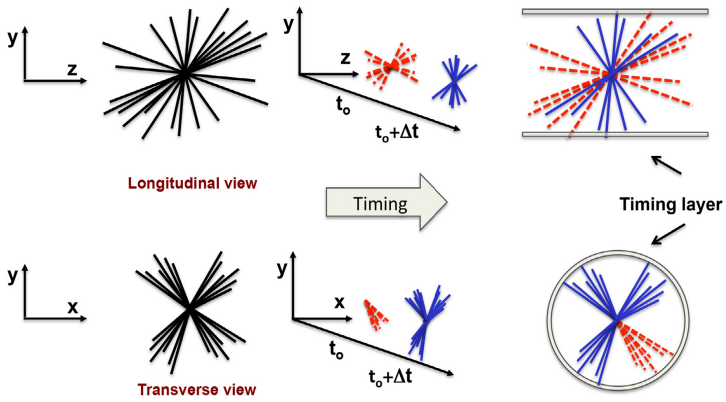

Figure 1.18: Timing information used to recognise overlapping events [6]

momentum $p >> m$:

$$c\Delta t = \frac{L(m_1^2 - m_2^2)}{2p^2} \tag{1.36}$$

it can be noted that when the momentum increases, the time difference decreases. When this becomes comparable with the time resolution of the detector, it is no longer possible to distinguish the particles. The separation in standard deviations n_σ between two particles given their mass m_i, their momentum p and the distance L of the TOF detector is:

$$n_\sigma = \frac{Lc(m_1^2 - m_2^2)}{2p^2\, dt} \tag{1.37}$$

where dt is the time resolution of the timing layer.

1.6.2 Other timing applications

4D Tracking

One or more timing layers with high performances are required in the ultra-high luminosity experiments, where the number of events per bunch crossing is so high to make the probability of merged vertex very high: the so-called "pileup". The time information provided by a timing layer allows assigning every single track, Figure 1.18, to the corresponding event, realizing what is commonly called 4D-Tracking.

As an example, in High-Luminosity LHC [12] the simulations predict a pileup for CMS [13] and ATLAS [14] that requires the introduction of dedicated timing layers. With 150-200 events per bunch-crossing [15] the introduction of a timing layer with a time resolution of 30 *ps* would lead to a reduction of a factor of 6 in the pileup [6]. The upgrades that will be made by the ATLAS and CMS, the experiments most affected by high pileups in HL-LHC, involve both the technologies that will be analysed in this work. In particular, CMS has decided to insert a timing layer composed of SiPM + crystals in

the barrel and LGAD in the endcaps. ATLAS, on the other hand, will insert 2 layers of LGAD detectors.

Medical PET

An important example of the application of fast silicon detectors outside the context of high energy physics is represented by the medical imaging system PET, Positron Emission Tomography. The method consists in the insertion of a radionuclide in a chemical substance used by a particular tissue or metabolic process. The β^+ decay of the radionuclide produces a positron which annihilating within 10^{-9} s produces a pair of 0.511 MeV photons emitted in opposite directions (conservation of momentum). Figure 1.19.

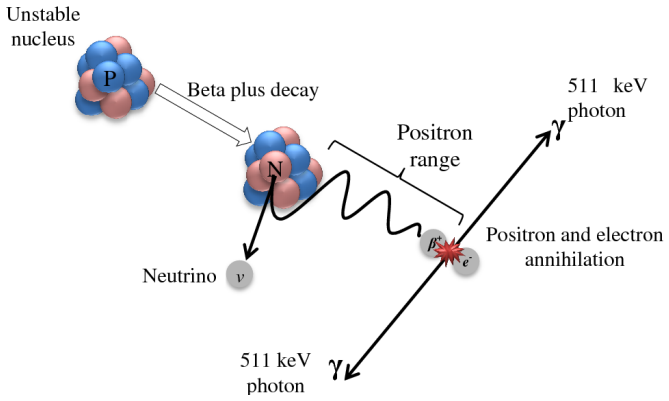

Figure 1.19: Positron emission and positron-electron annihilation processes [16]

The use of suitable detectors sensitive to the single-photon allows reconstructing the annihilation vertex making it possible to identify where the radionuclides have been accumulated. The first PETs were made by combining photomultipliers with scintillators. Subsequently, the introduction of TOF capabilities in these instruments allowed a huge improvement in the sensitivity and image quality of the recent TOF-PET together with a lower dose for the patient. In this context, the use of silicon detectors with excellent Timing and Single Photon Detection Efficiency (SPDE) capabilities was largely preferred, in particular SiPMs, illustrated in Section 1.4. The time resolution of the used detectors is strictly correlated with the ability to discriminate noise events from signal events [17], therefore this area of medical physics would also benefit from the development of ultra-fast SiPM.

Chapter 2

ALICE 3: a next-generation LHC heavy-ion experiment

ALICE 3 is a multipurpose detector, whose installation is expected during LS4 (Long Shutdown 4) in the IP2 interaction point, where the ALICE [18] experiment is currently located. The intent of this new generation detector is to use all the recent technological evolution in the field of ultra-thin silicon detectors in order to create an all-silicon tracker with a material budget of only 0.05% X_0 per layer [19]. This, combined with the insertion of the first vertexing layers inside the beam pipe, will allow to accurately study charged particles with a transverse momentum of few tens of MeV/c. In addition to the excellent vertexing capabilities, ALICE 3 will be equipped with one or more timing layers with extremely high time resolutions of the order of 20 ps.

The unique capabilities of tracking of the proposed detector will allow the study of AA, pA, and pp collisions with a luminosity 20-50 times larger than those achievable with the possible ALICE upgrades in Run3+Run4, opening the possibility to carry out, for example, high-precision measurements in physics of the open-heavy-flavour sector.

In this chapter, the detector layout will be briefly illustrated followed by a brief review of the technologies involved. Finally, the timing layer will be analysed in more detail as the main object of this work.

2.1 Detector layout

The proposed structure of the ALICE 3 apparatus is shown in Figure 2.1. The detector is extremely compact with longitudinal and radial dimensions of 4 m and 1.2 m respectively. It covers the pseudorapidity region of $|\eta| < 4$ over the full azimuth and consists of a central barrel plus two end caps. The whole experiment is surrounded by a solenoidal magnet, which will create a uniform magnetic field in the range between 0.2 T and 1 T. This will allow tracing particles with very low transverse momentum, few tens of MeV/c, while

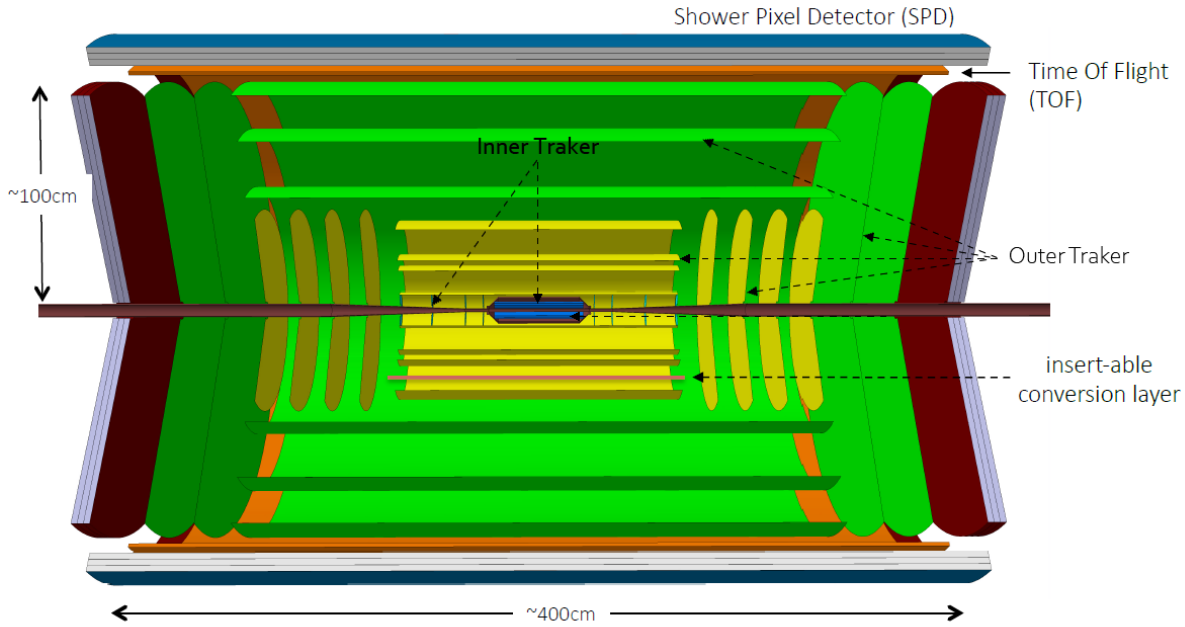

Figure 2.1: ALICE 3 proposed detector layout, adapted from [19]

maintaining a good resolution up to high transverse momentum, $p_t \sim 30\ GeV/c$.

The inner tracker (IT) will consist of 3 barrel layers inside the beam pipe, with the innermost positioned at 5 mm from the beamline, and 4 disks in the endcaps. A detail of the IT detector proposed can be seen in Figure 2.2.

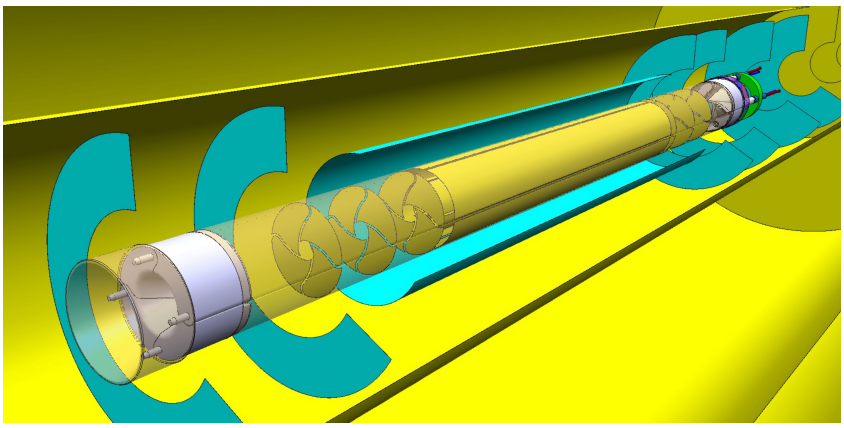

Figure 2.2: ALICE 3 proposed Inner Tracker IT system. In the figure, it is possible to see the first three layers of silicon detectors positioned inside the beam pipe and the subsequent ones surrounding it. From ALICE 3 workshop June 2021 [20]

The Outer Tracker (OT) will follow with 7 barrel layers, starting at a distance of 2 mm from the outer wall of the beamline, and 6 disks in the endcaps. in Figure 2.3, a simulation of the impact parameter resolution that will be achieved with the ALICE 3 experiment compared with that which will be obtained with the future ALICE upgrade with the introduction of ITS3 [21].

Immediately after the tracker system, the Timing Layer will be positioned and finally an electromagnetic Shower Pixel Detector (SPD) for the identification of photons and electrons with transverse momentum $p_t > 500\ MeV/c$ (SPD actual inclusion depends on the outcome of studies).

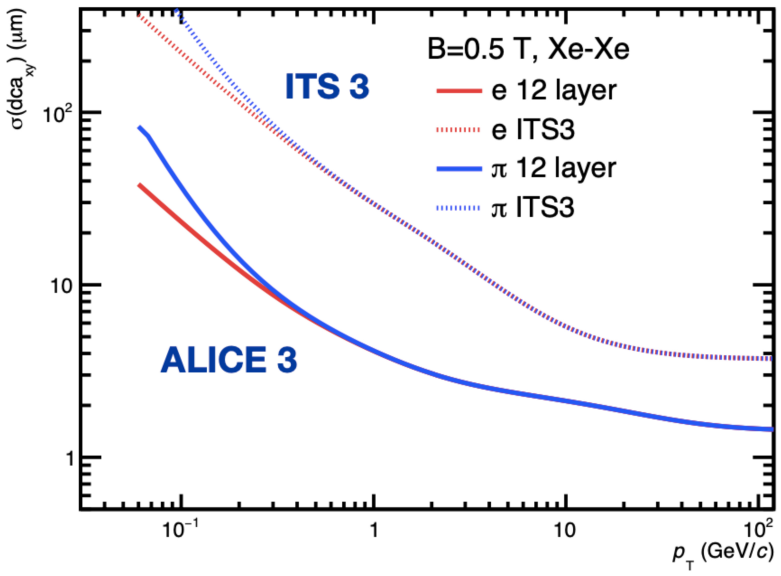

Figure 2.3: ALICE 3 Impact parameter resolution compared with that of the ALICE experiment after ITS3 installation. From ALICE 3 workshop June 2021 [20]

Also, the introduction of a RICH detector was proposed and discussed in the recent meetings of the ALICE 3 working group. Recent simulations have shown that the introduction of this detector, complementary to the TOF layer, would allow an Extensive particle Identification: e-π separation up to a moment of ~3 GeV/c, K-π up to ~10 GeV/c and p-K up to ~16 GeV/c.

The idea is to create a silicon timing layer capable of directly detecting charged particles but also single Cerenkov photons produced in an additional aerogel layer. In this context, SiPMs represent the best technology for the timing layer as they have been specifically designed for single-photon detection. In this context, a dedicated R&D must be done for the development of SiPM optimized for the detection of both: charged particles and single photons.

2.2 Technologies involved

As mentioned, the whole part of vertexing, tracking, and timing ALICE 3 will be based on ultra-thin silicon detectors technology.

Ultra-thin CMOS MAPS [22] wafers will be used for the Inner Tracker. This new and very promising technology (already used in the last ITS2 update of the ALICE experiment) consists in the production of large-size MAPS (up to 21 $cm \times 21$ cm) only 20-40 um thick. Thanks to the flexibility of these wafers, it is possible to produce cylindrical detector layers only 0.05% X_0 (radiation length) thick (ITS3, that will be installed in ALICE during the next update [21]). The sensor will contain 10^6 $pixels/cm^2$,each one with a size of 10 $\mu m \times 10$ μm allowing a spatial resolution of < 3 μm.

The same technology will be used for the Outer Tracker, where the size of the single-pixel will only be increased up to 30 $\mu m \times 30$ μm in order to reduce power density. This detector will allow reaching a spatial resolution of 5 um. Even the SPD, if introduced, will be based on silicon technology: thin layers of lead will be alternated with silicon detectors with high granularity. This will allow to analyse in detail the EM showers with very low pion contamination.

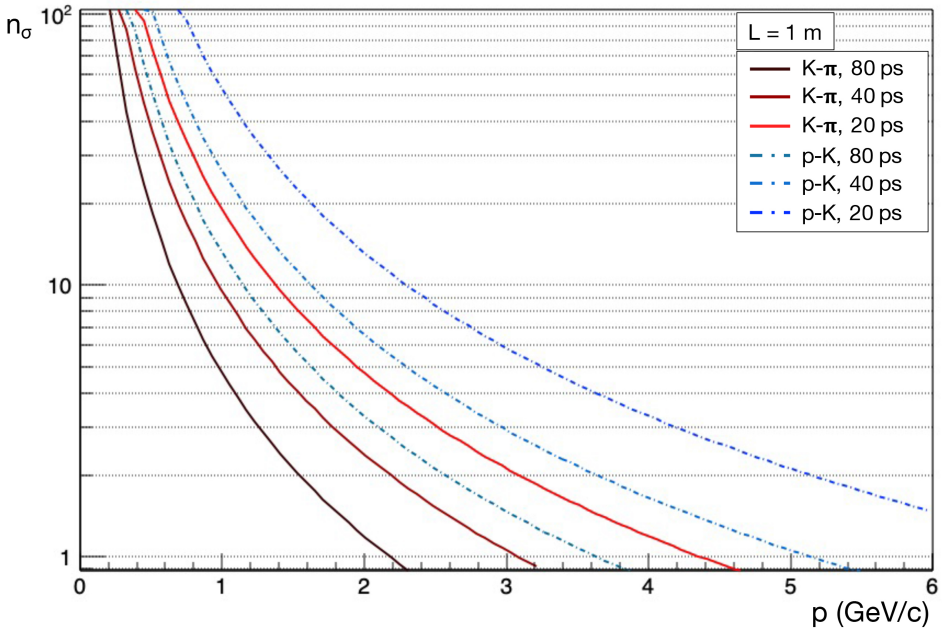

Figure 2.4: Simulated sigma separation in the ALICE 3 TOF [F. Carnesecchi, private communication].

2.3 Timing layer

As anticipated, one of the main technological challenges in the ALICE 3 experiment is linked to the production of a timing layer with time resolutions of the order of 20 ps. Such high performances are necessary to reach the PID objectives through the Time Of Flight technique required by the experiment. In the initial project, see Figure 2.1, it is planned to insert the timing detector at a distance of about 1 m. Using the relation 1.37 it is therefore possible to determine the separation in n_{sigma} between two particles of mass m_1 and m_2 using the TOF technique. In Figure 2.4 a simulation of the expected sigma separation for different time resolution values of the timing layer is reported. It is possible to note that, in the best of the hypotheses, if a time resolution of 20 ps will be reached, it will be possible to distinguish with at least 3σ p-K up to a moment of ~4 GeV/c, K-π up to ~2.5 GeV/c and e-π up to ~700 MeV/c. There are several candidate technologies for the timing detector. CMOS-MAPS, LGADs, and SPADs are the silicon technologies currently under study and have a good chance of achieving the 20 ps time resolution required by the experiment. Note that this should be the resolution of the entire detector and must include all contributions such as that of the readout electronics. No silicon detector has ever achieved such high timing performance while detecting MIPs until now.

Recent developments from the ALICE 3 working group, which is currently working in the drafting of a letter of intent, suggest the introduction of an additional TOF layer at 20cm from the IP. Table 2.1 summarizes the main characteristics required by the 2 TOF detectors, necessary to achieve the objectives of the future experiment.

	TOF at 20 cm	**TOF at 1 m**	**Note**
Pixel pitch	1 mm	5-6 mm	To keep the fake match probability < 1% and e/π misidentification <1E-3
Hit rate $[kHz/cm^2]$	3.7E+3	1.5E+2	O-O at $\mathcal{L}_{max} = 9.43\,E + 31$ cm$^{-2}s^{-1}$
NIEL $[1MeVn_{eq}/cm^2]$	2.31E+12	9.24E+10	Per month, considering O-O at $\mathcal{L}_{avg} = 4.54\,E + 31$ cm$^{-2}s^{-1}$
AREA$[m^2]$	1.56	25.13	Assuming L(20cm)=1.24 m and L(1m)=4 m
Time Resolution [ps]	<50	20	The TOF layer at 20 cm will be used for low momentum PID, lower timing performances are therefore required.

Table 2.1: Preliminary requirements of the two TOF layers for the ALICE 3 experiment [A. Alici, S. Bufalino, A. Rivetti, private communication].

Chapter 3

SiPM studies in cosmic rays and laser setup

After a brief description of the devices used in this thesis work (Section 3.1), some preliminary measurements will be reported (section 3.2). The time resolution measurements of the Hamamatsu (HPK) SiPM S13360-3050V exposed directly to Cosmic Rays (CR) will be presented (Section 3.3). A complete characterization of the device was carried out using a 1054 nm pulsed laser, the results of these studies will be reported (Section 3.4). An unexpected result inherent to the crosstalk of the device will be discussed (Section 3.5). Then the CR and Laser results will be compared (Section 3.6). Finally, the preliminary time resolution results of FBK SiPMs prototypes will be illustrated (Section 3.7).

This study represents a novelty in the field of possible SiPM applications: for the first time, here, the intent is to study the tracking and timing performance of SiPMs in the direct detection of MIP and not photons (as in all other standard applications of these devices). The in-depth characterization of SiPMs with the 1054 nm laser also led to interesting results.

3.1 Devices and characteristics

In this thesis, several prototypes and commercial devices have been studied in order to determine their main characteristics and, in particular, the time resolution. The goal is to identify which technology, and in which configuration, is best suited for use as a detector of the timing layer in the future ALICE 3 experiment. In Table 3.1 the list of the devices studied with their main characteristics, in particular the different hexagonal or square shapes of the SPADs. From now on we will refer to them using the ID reported here. Microscope photographs of the devices are shown in Figure 3.1.

All four different types of SiPMs were tested with laser and compared. With the SiPM

Factory	Active Area	Pixels shape and pitch	ID
HPK	$3\ mm \times 3\ mm$	Square, 50 μm	HPK-S13360-3050VE
FBK	$1\ mm \times 1\ mm$	Hexagonal, 20 μm	FBK-SiPM-6
FBK	$1\ mm \times 1\ mm$	Square, 15 μm	FBK-SiPM-7
FBK	$1\ mm \times 1\ mm$	Hexagonal, 15 μm	FBK-SiPM-8

Table 3.1: Tested SiPMs.

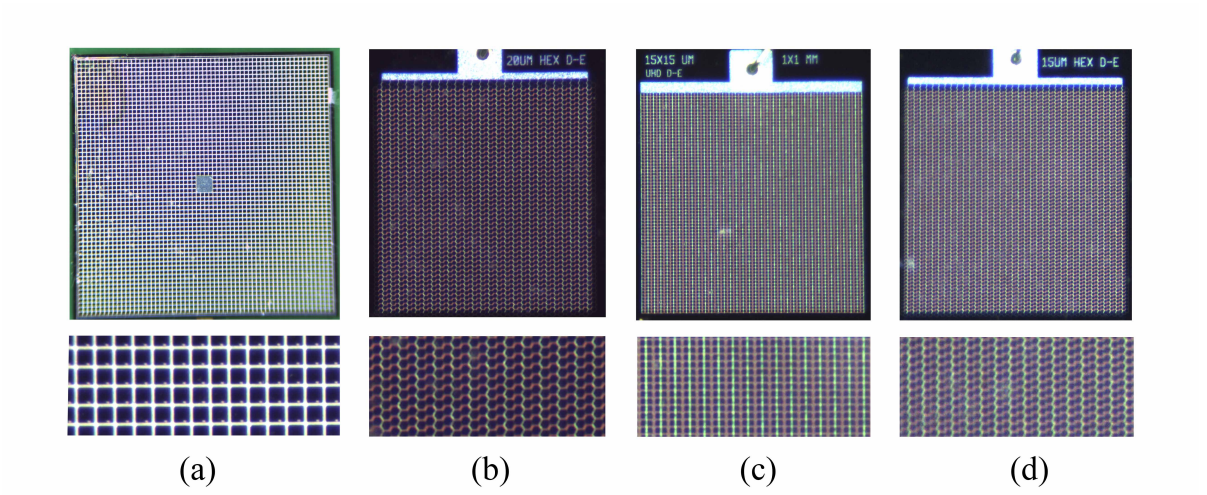

Figure 3.1: Microscope photographs of the tested devices. SiPM HPK-S13360-3050VE (a), FBK-SiPM-6 (b), FBK-SiPM-7 (c), FBK-SiPM-8 (d).

S13360-3050VE produced by the Hamamatsu Photonics K.K. (HPK) factory, optimized for medical imaging and high-energy particle detection [23], it has been done also a study with cosmic rays to test its performance as tracking timing detector for charged particles. Being a commercial device, more detailed specifications are available: in Table 3.2 some of the main characteristics of the detector are shown.

3.1.1 IV curves

The most important, necessary, characterization of this type of silicon detectors consists in the IV curve of the device (which, in these cases, can be seen as a reverse-biased diode). This allows determining the optimal working conditions of the device at a given temperature. In particular, for SiPMs, it is important to determine the breakdown voltage V_{bd} at which the device enters in Geiger-mode (Section 1.3.3). Figure 3.2 shows the IVs of the tested SiPMs obtained with the TDK-Lambda Z100-2 power supply and

Effective photosensitive area	3 × 3 mm
Number of pixels	3584
Pixel size	50 μm
Peak sensitivity wavelength	450 nm
Gain ($V_{BR} + 3V$)	1.7×10^6
Recommended op. voltage	V_{BD} +3 V
Fill Factor	74%

Table 3.2: SiPM HPK S13360-3050V main technical parameters, from [23].

the Keithley 6487 picoammeter (Appendix: Instrumentation). The SiPM is always used few volts above the breakdown voltage (see Section 1.4.1). Generally the time resolution of a SiPM change with overvoltage, it is therefore essential to evaluate it for different VBIAS in order to find the optimal working conditions (few volts above the V_{bd}). For the HPK sensor, a V_{bd} of ~52 V was found on all three tested samples. For all FBK prototypes the V_{bd} is ~33 V.

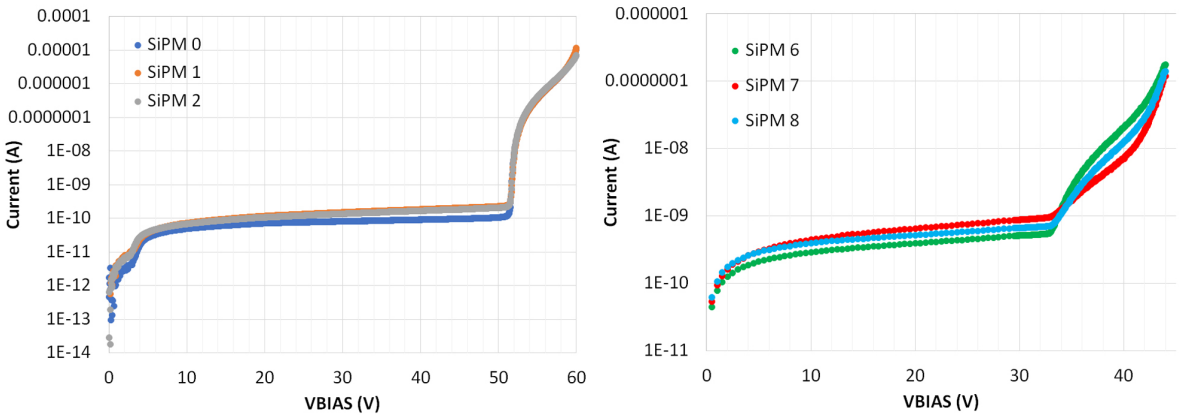

Figure 3.2: IV curve of all tested SiPMs HPK-S13360-3050VE (left). IV curve of the FBK SiPMs tested (right).

3.2 LabVIEW program for automatic laser scan of devices

Many of the results presented in this work have been obtained using a picosecond pulsed laser with a wavelength of 1054 nm. To this purpose was developed a LabVIEW [24] program to allow an automatic scan of the studied sensor, allowing an evaluation of the

entire light-sensitive area in terms of efficiency, time resolution, presence of any defects, edge effects, etc.

3.2.1 Setup description

In Figure 3.3 the setup scheme is represented. The studied sensor is positioned vertically on a 2 axes Micrometer Positioning Stages (MPS) (Standa 8MT167-25LS) and the readout signals are connected to a digital oscilloscope. MPS and sensor (with amplifier) are placed inside a dark box. The laser light used for the studies, produced by the PILAS 1054 nm laser (PiLas PiL036XSM head + EIG2000DX controller), enters the box through a single-mode optical fiber (Torlabs P3-980A-FC-1) and is then collimated (Schäfter+Kirchhoff 60FC-T-4-M40-54) and focused in a micrometric spot by the Schäfter+Kirchhoff lens (Micro Focus Optics 13M-M40-54-S). This last optical group is mounted on a micro-moving device (manually controlled). This controls the distance of the focusing lens from the sensor with an accuracy of up to 20 μm, allowing the correct focusing of the laser spot. The LabVIEW program controls the MPS giving the possibility to set the scan area, x and y step between adjacent points and measurement time at each coordinate. For each position, the software acquires (after waiting the set time, useful for improving the measurement statistics) the measurements made by the oscilloscope, storing them on a text file for future analysis (the digital oscilloscopes used, allows live measurements and analysis on the input data; each type of measurement that can be carried out by the oscilloscope, as the maximum amplitude of the signal in a chosen region, can be stored by LabVIEW program). Three different Teledyne LeCroy oscilloscopes (WaveRunner 104MXi, WaveRunner 9404M-MS, WaveMaster SDA 816Zi-A) have been used in various applications; for greater stability in the connection, it was decided to use the communication via crossover network cable between PC and oscilloscope.

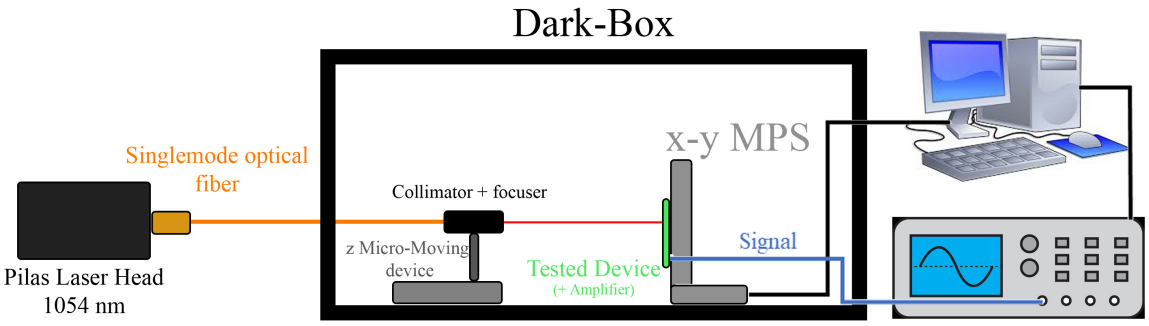

Figure 3.3: Laser Setup for automatic scans of devices.

3.2.2 Laser preliminary studies

Preliminary tests on a 2x2 matrix of LGAD

As anticipated, in the study of prototypes it is often useful to check the uniformity of the detector response in different active areas of the sensor. An x and y step scan of 100 μm step was performed on the entire surface of an LGAD matrix prototype produced by the FBK using the setup described above. It was decided to use this detector in the development and calibration phases of the LabVIEW program and for the test of the procedures, because it has a very large 1054 nm laser light-sensitive area (four pixels with 1.5 $mm \times 1.5$ mm of exposed surface). The result is shown in Figure 3.4. As can be seen, each pixel produces a signal that stays almost uniform over the entire light-exposed area. The differences in amplitude of the signals produced by the 4 pixels are due to a non-uniform operation of the preamplifier stages mounted on this prototype (already known from previous studies)[25].

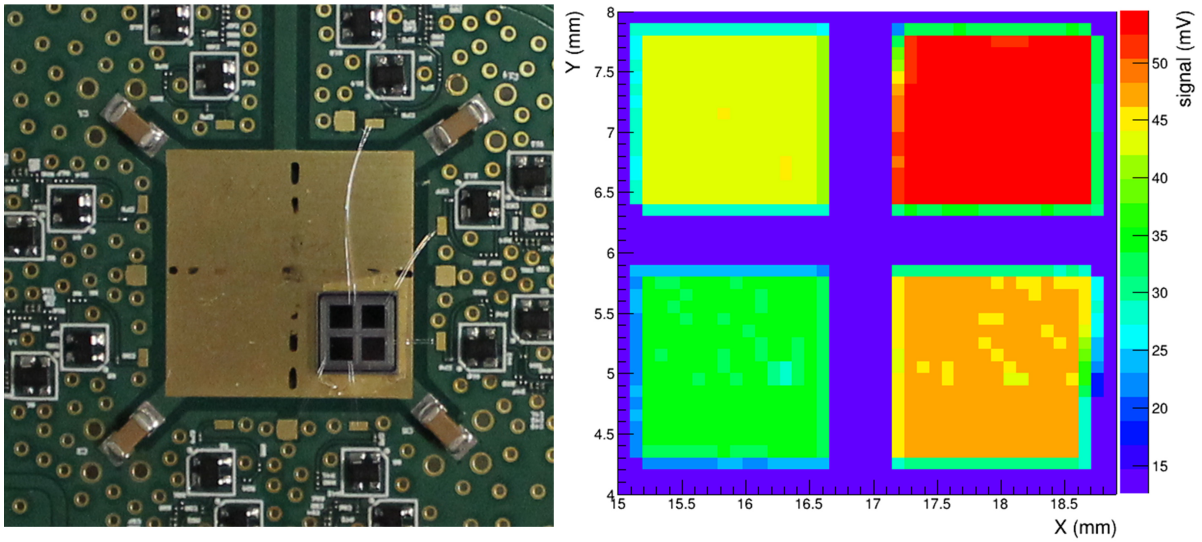

Figure 3.4: FBK 2x2 Matrix of LGAD (50 µm tecnology) prototype with preamplification stages (left). Signal recorded on the entire sensor with automatic scan.(right)

Determination of the laser spot size

Many of the studies, reported in the next chapters, were carried out on single SiPM SPADs. It was therefore necessary to determine the size of the focused 1054 nm laser spot in order to be sure of directing the light onto a single SPAD without directly hitting the adjacent ones. The spot, properly focused, has a circular Gaussian-shaped intensity

maximum in the central point. Several horizontal scans were performed involving the transition zones between blind sensor areas and active areas to determine the sigma σ_G of this Gaussian. In these regions a transition in the output signal is expected that follows a pattern described by the function:

$$Signal = \frac{A}{2}[1 - erf(\frac{x - x_0}{\sqrt{2}\sigma_G})] + Const. \tag{3.1}$$

This function is the convolution of a step function of amplitude A (which schematizes the transition between the active and the blind area of the sensor) and a Gaussian of mean x_0 and sigma σ_G that represents the laser spot intensity distribution.

In Figure 3.5 the result of two different scans is reported. The first (left) was performed in the SiPM blind area (described in the next example of this paragraph). The second (right) was, instead, measured on an LGAD sensor 2x2 Matrix (previous example) in a transition region between the active area and the metallization between pixels, with different laser light intensities.

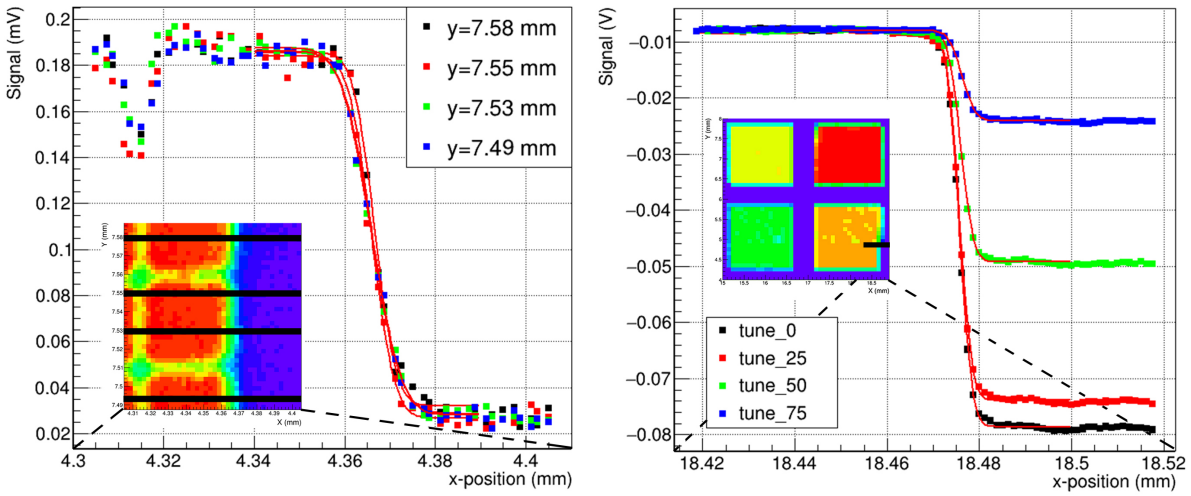

Figure 3.5: Horizontal scans carried out in the central area of the SiPM HPK-S13360-3050VE to determine the laser spot size (left). Scanning was performed between the active and blind area of an LGAD matrix as a function of laser light intensity (right). Here a tune is applied to the laser light: Tune 0 corresponds to the maximum light intensity. In both cases, a horizontal black line indicates the approximate region of the scan.

In Table 3.3 the sigmas σ_G extracted fitting data with the Function 3.1 are reported. It can be noted that the sigma extracted using the LGAD, which essentially does not change for different laser light intensity, is smaller than that extracted using the SiPM. This is because the SiPM, being sensitive to the single-photon, produces a signal even

Scan ID	Fitted σ_G
SiPM (Black)	3.7 ± 0.8 μm
SiPM (Red)	3.9 ± 0.8 μm
SiPM (Green)	5.2 ± 0.7 μm
SiPM (Blue)	5.1 ± 0.7 μm
LGAD (Black)	2.18 ± 0.03 μm
LGAD (Red)	2.14 ± 0.03 μm
LGAD (Green)	2.15 ± 0.04 μm
LGAD (Blue)	3.31 ± 0.06 μm

Table 3.3: σ_G extracted from the fits in the Figure 3.5.

when hit by the less intense edges of the laser spot. LGAD, on the other hand, requires a greater number of photons to produce an appreciable signal and is therefore sensitive only to the most intense core of the laser spot. It should be noted that the correlation between the σ_G extracted in this way and the actual total spot size could be affected by the tails of the Gaussian that, in very intense light conditions, could be more populated. However, given the measurements, we can deduce with a good confidence level that the spot size is of the order of 10 μm (twice of the maximum fitted σ_G).

Signal of a portion of the SiPM HPK-S13360-3050VE

As described in Section 1.4, a SiPM consists of an array of single SPADs read in parallel. The SiPM HPK S13360-3050VE, has 3584 $50 \times 50\,\mu m^2$ SPADs. The spot size of the Infra-Red (IR) laser used in the setup is estimated to be of the order of 10 μm (see the previous example in this section), thus 5 times below the dimension of the SPAD pitch. Figure 3.6 shows the automatic signal scan result of a portion of the SiPM made with an XY step of 2 μm, where the output signal is amplified by a factor 100 by the Cividec C2-HV Broadband Amplifier (each point represents the average of the measurements on exposure of 10 s, ~1k events). The measurement was performed in a position where the anode is placed (in the middle of the sensor) and it is possible to appreciate in Figure 3.6 the transition between the active area of the sensor and the laser blind area. It can be seen that the single cell is clearly distinguishable, with the signal decreasing (on average) in the areas between adjacent SPADs (blind regions of the sensor). It can be seen as in these areas, where ideally there should be no signal, only a decrease in the average sensor response is observed (visible also in Figure 3.5 (left)). This is due to the laser spot size comparable with the size of this blind area, which at these coordinates, although less likely, can trigger one or more adjacent cells.

Another similar scan was performed on the SiPM FBK-SiPM-6. The result is shown in Figure 3.7. The hexagonal cells are clearly distinguishable, however, in this case, the

signal increases in the intersection areas between cells. This is due to the size of the spot, which in this case is greater than the blind area between adjacent cells and so the signals from two or more cells are summed.

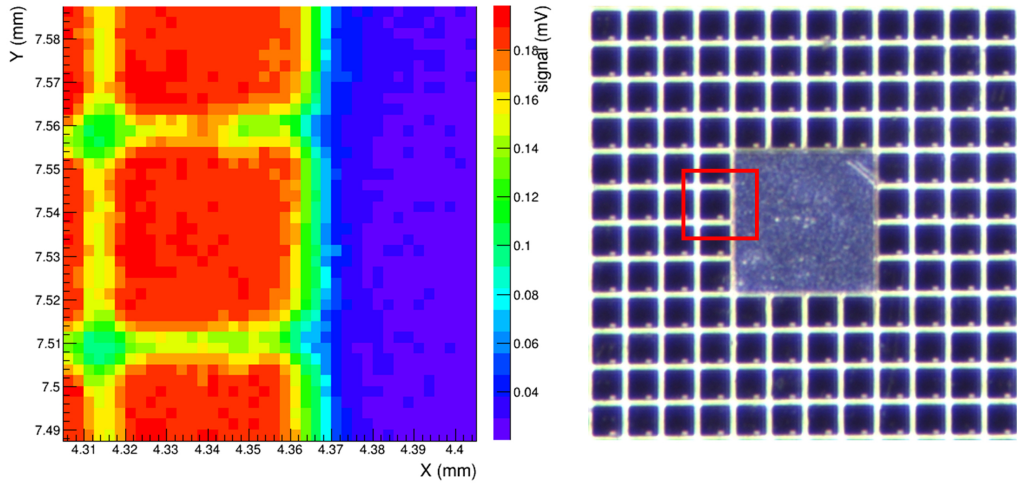

Figure 3.6: Automatic signal scan result of a portion of the SiPM HPK-S13360-3050VE (left). Microscope detail of the area used for the scan (right). Note that there are no SPADs under the metallic central part (anode).

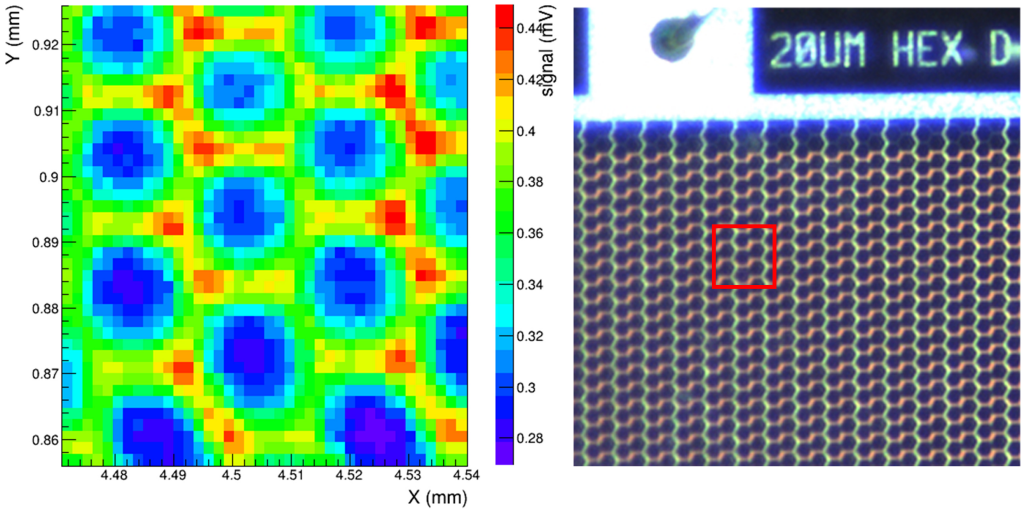

Figure 3.7: Automatic signal scan result of a portion of the SiPM FBK-SiPM-6 (left). Microscope detail of the area used for the scan (right).

3.3 First studies of SiPM directly detecting MIPs

The SiPMs have always been used as light detectors. Also in the context of the detection of charged particles they are widely used coupled, for example, with scintillator materials replacing the classic photomultipliers [26]. However, to our knowledge, no reference in the literature has been found regarding SiPMs directly used in the detection of MIP without any type of coupling with scintillator materials. This study, and more generally the studies of the group focused on the development of the ALICE 3 timing layer, can be considered the first of this type.

3.3.1 Setup

The setup used to study the resolution of HPK SiPMs directly detecting cosmic rays is shown in Figure 3.8. Three SiPMs were vertically aligned in a 3D printed structure making a Cosmic Rays Telescope. The SiPMs were powered with the circuit shown in Figure 3.9 and their signal was amplified by 20dB using a Cividec C2-HV amplifier. Below them, a scintillator coupled with a SiPM was used as a trigger. The whole setup was placed inside a wooden dark box at a constant temperature of 22±2 °C. The 3

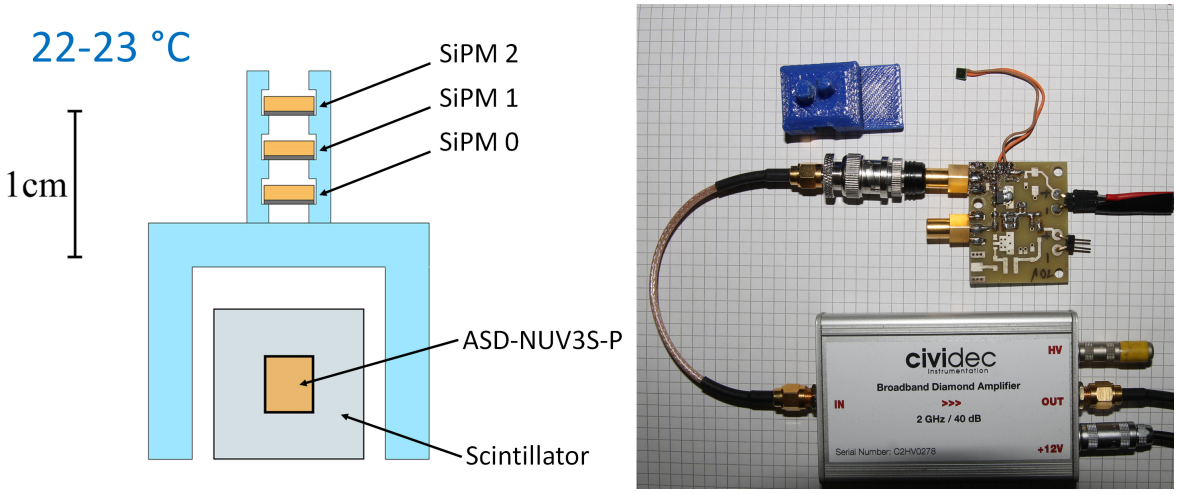

Figure 3.8: CR Telescope Setup with SiPM directly detecting charged particles. Schematic representation of the CR telescope (left). Photograph of one of the SiPMs tested with biasing and readout circuit, amplifier and 3D printed support (right). Note that the blue part in the figure (left) represents the PLA material of the 3D printed support.

SiPMs were powered in parallel by the power supply TDK-Lambda Z100-2 and their amplified signals, together with that of the SiPM ASD-NUV3S-P [27] with the plastic scintillator BC-420 [28] used as trigger, were read by the Wave-Master SDA 816Zi-A oscilloscope. At each trigger event, the oscilloscope saved the entire waveforms of the 4

signals for subsequent analysis. It was decided to limit the bandwidth of the oscilloscope to 200 MHz, thus ensuring a good Signal/Noise ratio in all the tests carried out. For the sampling rate, on the other hand, the oscilloscope was exploited at full power using the maximum sampling capacity at 40Gs/s on all four channels, guaranteeing a resolution between consecutive points of 25ps.

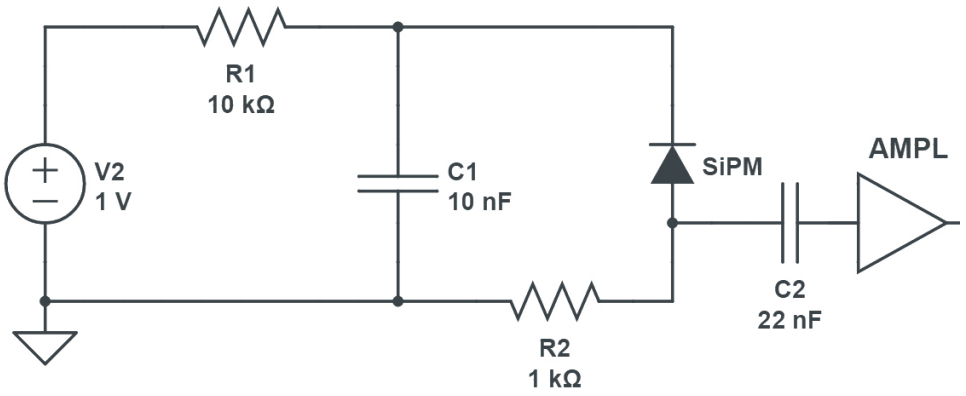

Figure 3.9: Circuit used for biasing and readout SiPM HPK-S13360-3050VE.

3.3.2 Signal Selection

The measurements made with the CR setup required several months of data taking. As visible in Figure 3.8, the scintillator used as a trigger covered a much larger area than the SiPM surface. This was decided to minimize the possibility of not having a trigger event when a cosmic ray passed through one or more SiPMs. Consequently, many of the trigger events were triggered by CRs that did not produce a signal in any of the 3 SiPMs. To evaluate the time resolution of the studied SiPMs, cuts were applied in order to select only the cosmic ray signal events. Here is a list of the cuts used for the selection applied, separately, on each of the three SiPMs:

- As the first main selection, all the events in which the SiPM did not exceed the chosen threshold (depending on the voltage used) in a window of ± 10 ns from the trigger condition were excluded.

- Many dark-count events, in the window of ± 10 ns from the trigger, were not rejected by the first selection. Also other particularly large electronic noise events (such that exceed the chosen threshold) passed the first selection. To improve the selection, a particular type of pulse shape analysis was carried out [29]. Starting from the oscilloscope output file, for each i.th signal point the quantity δ_i is

computed by using the equation:

$$\delta_i = \sum_{k=1}^{N} s_{i+k} - \sum_{k=1}^{N} s_{i-k} \tag{3.2}$$

Where s_i is the signal of the i-th point and N a suitably chosen integer. Note that, even if related, this is not the classical derivative dV/dt (as this would have been too prone to fluctuations due to electronic noise) but it is a quantity obtained by subtracting from each other the integral of the signal calculated discretely on N points from both sides of the i-th point. The result is a smoothed "derivative" that is easier to handle and differs by a constant from the classical derivative. An example of the signal with the relative derivative calculated with the previous method using $N = 40$ is shown in Figure 3.10 (given the sampling speed of the oscilloscope, this corresponds to an average over a time of 1 ns). The derivative obtained was fitted with a Gaussian curve in the trigger region (time 0 in Figure 3.10), it was, therefore, possible to make cuts on the sigma and the amplitude of this fit (when it converges) and obtain a perfect separation between signal and noise events. Note that the δ_i described was used only to facilitate the selection of signal events; the analysis to extract the SiPM time resolution described in the next section, on the other hand, was done directly with the signal.

- In order to preserve the resolution on the signal, a suitable scale was chosen on the y axis of the oscilloscope; and as a consequence in some cases (also due to unexpected excessive crosstalk, which will be discussed later) the signal saturated and therefore it could not be used for the analysis. All the saturated events in the chosen scale were therefore excluded from the analysis (few events compared to the total).

A final cut was made by looking at the signals of all three SiPMs at each trigger, requiring that at least 2 of the SiPMs had produced a signal in the chosen window not rejected by previous cuts (necessary for the analysis that will be illustrated in the next paragraph).

An example of selection is shown in Figure 3.11, on the left all the events stored as a result of the trigger condition, on the right only the events selected after having made all the cuts described. In the Figure 3.11 it is possible to clearly distinguish signals due to single SPAD events (in greater number with a maximum amplitude of the first peak of about 200 mV) and signals due to events with crosstalk involving two, three, and four cells (as well as some saturated events). Events with afterpulsing and Dark Count (DC) events are also distinguishable (see Section 1.4.3). The events with correlated noise (Section 1.4.3) after the signal peak, not compromising the time resolution measure, were not excluded.

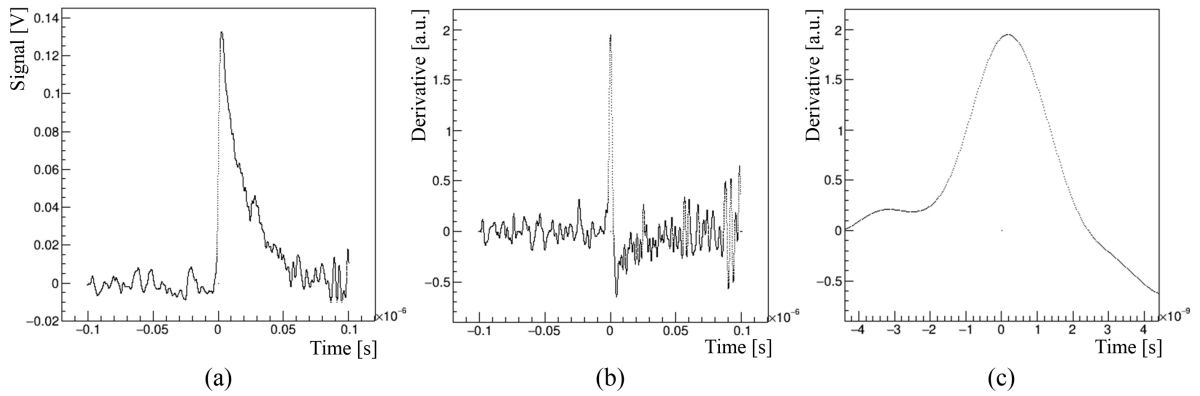

Figure 3.10: Example of SiPM Signal (a), and its Derivative (b) with a detail of Gaussian shape in the region of peak (c). Note that in figure (c) the time scale is 1000 times expanded: region around time 0 (trigger condition) is shown where the signal is expected.

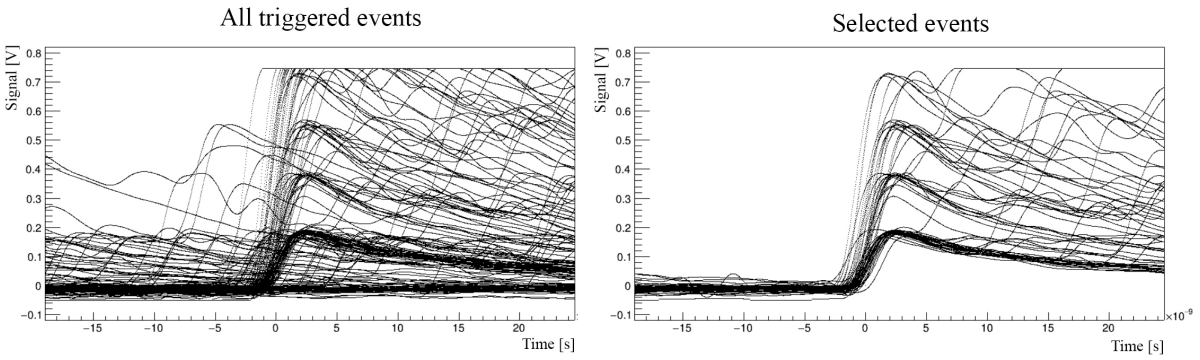

Figure 3.11: Example of SiPM signals selection in CR Setup.

3.3.3 Extrapolation of the intrinsic time resolution

In order not to depend on the time resolution of the trigger detector, it was decided to measure the resolution of the SiPMs considering, as anticipated, cosmic ray events that had hit at least two of the three SiPMs of the Setup (Figure 3.8). The scintillator, the main trigger, was then used only for selecting CR events. To evaluate the time resolution it was decided to use the Constant Fraction Discrimination method (CFD) [30]: given the signal of a SiPM, it is evaluated the time when this exceeds a certain percentage threshold with respect to the maximum amplitude of the signal. The distribution of these times is generally Gaussian; the sigma of the distribution is therefore directly related to the time resolution of the detector.

Before proceeding to the determination of the time resolution, a slewing correction was carried out; usually, the total deposited charge is used for the CFD analysis, however,

in the case of SiPM, the presence of events with correlated noise can make the method inaccurate; use the maximum amplitude of the first peak of the signal is, therefore, the best choice. It was then decided to apply a slewing correction by removing the correlation between the signal amplitude and the time in which the chosen Constant Fraction is reached, Figure 3.12.

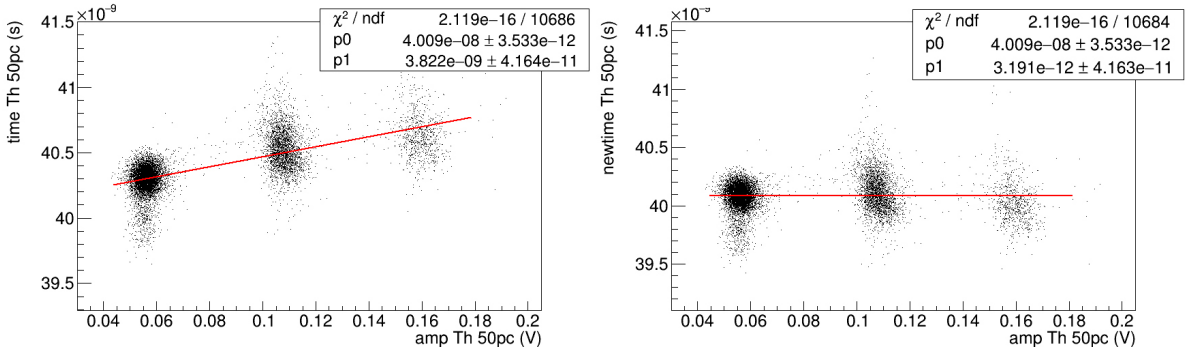

Figure 3.12: Example of Time slewing correction. In the figure is plotted time of CFD 50% vs amplitude of signal, before (left) and after (right) correction. Parameters of a linear fit are also reported. Note that each group of point correspond to one, two or three SPADs events (direct crosstalk).

As stated, having no reference trigger, the time resolution of the devices was then determined by subtracting from each other the times when the signals of the two considered SiPMs, exceeded the percentage threshold. The times thus obtained will be generally Gaussian distributed; the sigma σ_{diff} of this will therefore be related to the resolution of the single SiPM σ_{SiPM} by the equation:

$$\sigma_{SiPM} = \frac{\sigma_{diff}}{\sqrt{2}} \tag{3.3}$$

Note that we are assuming the two SiPMs as identical. σ_{SiPM} thus obtained represent the time resolution of the detector. An important contribution here is represented by the electronic jitter, related to the sensor+amplifier combination. Given the size of the SiPM (and therefore its large capacity), this is a significant contribution. As reported in the Equation 1.25, in order to extract the intrinsic time resolution it is necessary to subtract the contribution of the electronic noise jitter σ_{Jitter} (Equation 1.23) and the therm related to the TDC σ_{TDC} (Equation 1.24) (negligible due to the Wave-Master SDA 816Zi-A TDC_{bin} of 25 ps).

3.3.4 Results

About five months were needed to collect the necessary data for the first, preliminary, conclusions. As an example of experiment results, in Figure 3.13 is reported one of the

histograms resulting from the analysis of the difference in time of the pair of SiPMs 0-2 with VBIAS of 55.5V choosing a CFD of 50%. The standard deviation extracted from the Gaussian fit corresponds to the σ_{diff} value used in the Equation 3.3. Table 3.4 shows the result of the analysis for the 3 tested VBIAS values. The table shows the numbers of coincidences counted for the three possible pairs of the SiPM for the 3 tested VBIAS. The CFD 50% value was chosen in the final selection, as it corresponded to the threshold which, in most subsets of data, returned the best TR. The time resolutions obtained for the three pairs combination were then merged with a weighted average (considering the number of events selected with the different pairs of SiPMs, Table 3.4) and the intrinsic resolution was extracted using the Equation 1.25, the jitter values are reported in Table 3.4 and the TDC contribution can be considered negligible. Note how the 53V value, due to the low signal to noise ratio of the measurement, has an overestimation of the Jitter term; it was therefore not possible to estimate the intrinsic time resolution (a topic discussed in the following paragraphs).

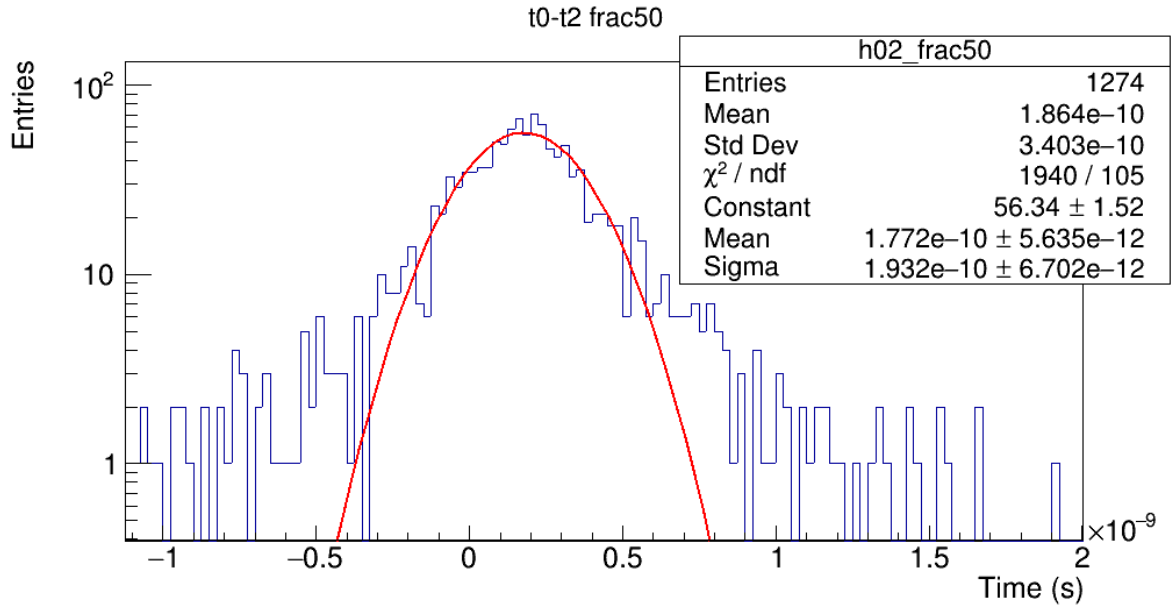

Figure 3.13: Time to exceed the CFD threshold of 50% for the SiPM 0-2 pair in CR setup with VBIAS of 55.5V. The sigma of the fitted Gaussian corresponds to σ_{diff}. Less than 10% of the events are in the tails.

As can be seen, it was decided to increase the statistics more for the average voltage value of 55.5V; in this case, the intrinsic time resolution of the SiPM HPK S13360-3050VE directly detecting charged particles is just over 100 ps. For higher values of over-voltage, the time resolution measured with the setup remains identical, however, due to a greater contribution in the jitter term, the extraction of the intrinsic resolution

VBIAS [V]	events SiPMs 0-1	events SiPMs 0-2	events SiPMs 1-2	Tot. events	Measured TR [ps]	Jitter [ps]	Intrinsic TR [ps]
53.0 ± 0.1	365	228	247	840	181 ± 30	167 ± 13	–
55.5 ± 0.1	1693	1274	1113	4080	149 ± 17	93 ± 6	113 ± 27
58.0 ± 0.1	585	412	353	1350	150 ± 25	121 ± 9	85 ± 42

Table 3.4: Results of the measurements with CR. For the different VBIAS tested, the number of signal event counts for the different possible SiPMs pairs is reported. In the last two columns the measured time resolution, jitter therm and derived intrinsic time resolution. All events (single and multi-SPADs) were used in the analysis.

leads to a measured value of about 85 ps. Figure 3.14 shows graphically the results of the analysis with errors.

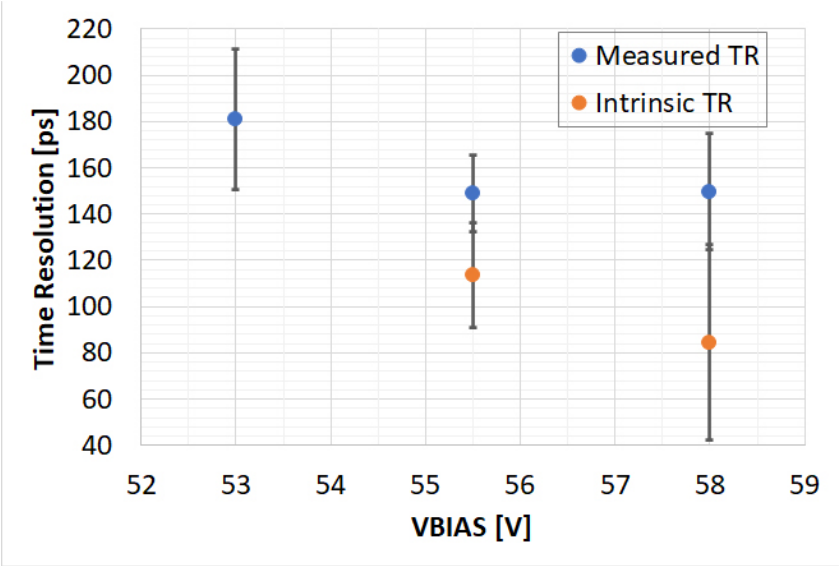

Figure 3.14: Measured and intrinsic time resolution of the SiPM HPK S13360-3050VE directly detecting Cosmic Rays (It should be noted that for the VBIAS value of 53 V it was not possible to extract the intrinsic time resolution due to the low Signal/Noise ratio). All events (single and multi-SPADs) are included in the analysis.

The errors in the measurements are still very large due to the low statistics and more points would be advisable in order to better compare the results with those described in the next section.

The results presented in this section have to be considered preliminary. To improve the statistics of these measurements and to extend this type of charged particle stud-

ies to other SiPMs prototypes, a beam test is scheduled for next autumn (at Proton Synchrotron (PS) at CERN).

3.4 Laser studies on HPK SiPM

The tests with CR, given the small size of the HPK SiPM under examination, required several months of data taking and, despite this, the statistics, as mentioned, are not sufficient to draw certain conclusions. It was therefore decided to also study the SiPM using a 1054 nm pulsed laser.

The use of focused 1054 nm IR laser light, is a good choice to compare the laser studies results with those obtained in the measurements with CR presented in the previous section. In fact, IR light can penetrate several tens of μm producing e-h pairs in the silicon at different depths (depending on where the photons of the beam interact) with a mean absorption depth reported in Figure 1.7. A MIP, on the other hand, produces e-h pairs along its entire path with a rate of about 73 pairs for each μm crossed [6]. Not knowing the thickness of the SiPM active area, and being the number of pairs created by the laser light difficult to evaluate in these sensors, time resolution studies with different laser beam intensities have been carried out (see next section).

The same setup described in Section 3.2.1 with the Wave-Master SDA 816Zi-A oscilloscope was used for the measurements described in this chapter. The SiPM, powered with the same circuit shown in Figure 3.9, and amplified again with the Cividec 20dB amplifier, was, in this setup, enclosed in a Faraday-box made using a 3D printed PLA case suitably covered with copper tape (Figure 3.15). This made it possible to remove most of the laser setup electromagnetic noise obtaining an excellent signal/noise ratio comparable with that of the low noise CR setup.

The main objective of these laser studies was to develop all the tools, measurement, and analysis techniques necessary to prepare some of the prototypes for the charged particle beam test that will be carried out at CERN in autumn and subsequent laser comparison studies in the INFN laboratories in Bologna.

3.4.1 Time resolution of a Single SPAD in the SiPM

A charged particle that hits the HPK SiPM perpendicularly (which we recall has pixels of area $50\mu m$ x 50 μm and a Fill Factor of 74%) generates primary pairs, almost always, in a single SPAD since the sensitive surface is much greater than the thickness of the active area and since the setup geometry used (see Figure3.8). With the laser setup, the behavior of the single SPAD in the SiPM array was studied by focusing 1054 nm laser light in a micrometric spot.

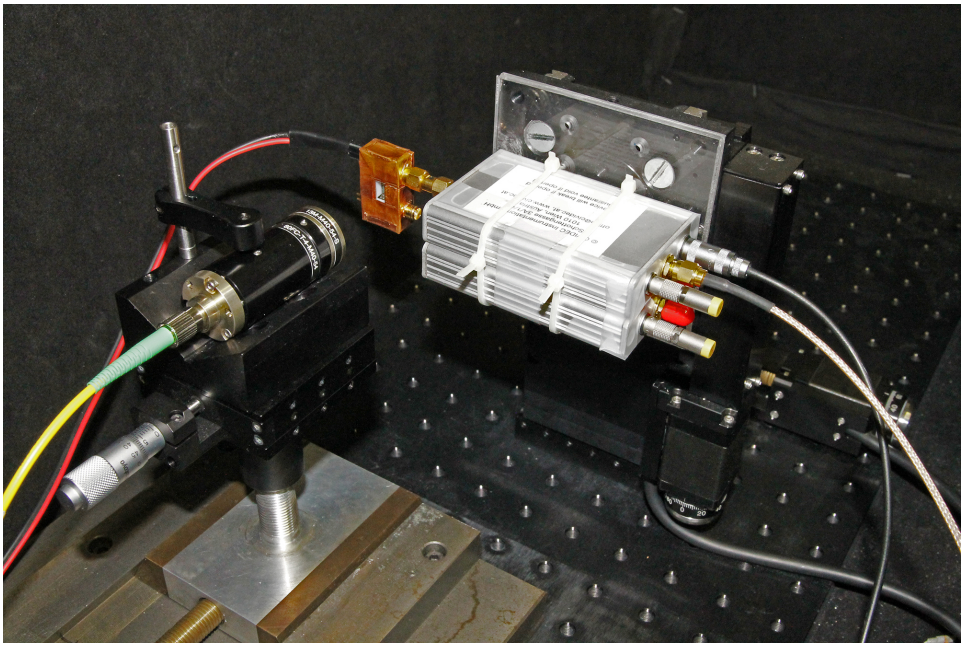

Figure 3.15: Photograph of the setup for laser measurements. It is possible to distinguish the copper-clad box (which contains SiPM and biasing-readout electronics) directly connected to the Cividec amplifier, mounted on the x-y MPS axes. The laser light enters the dark-box through the optical fiber (in yellow) which is directly connected to the collimator + microfocuser pair. The optical unit is mounted on a manually controlled micro-mover z-axis.

Time resolution as function of overvoltage

By randomly choosing one SPAD within the SiPM, we first verified to be in the best laser focus conditions to ensure illuminating a single SPAD. Scans similar to those shown in Figure 3.6 have been performed to check the laser spot size. Positioning the laser at the center of the SPAD, the time resolution of the single SPAD was then evaluated as a function of the overvoltage, using the maximum amount of light that can be delivered by the setup (note that, due to losses in the fiber connections and to the calibration of the setup that is not perfect, this light is to be considered lower than that produced by the PiLas laser head). The data were analyzed in a similar way to what is described in Section 3.3.3 using the CFD method. This time, however, since a single SiPM was involved, the trigger provided by the power supply of the laser was used as a reference; the jitter of this device was evaluated to be negligible compared to the measurement. About 15K events were analyzed for each voltage value and of these, in this first phase of the study, only events corresponding to a single triggered SPAD were selected (Figure 3.16 left), discarding, in this first phase of the analysis, the events with direct crosstalk;

that is, in the example shown, those with peaks greater than 0.2 V in Figure 3.16(right).

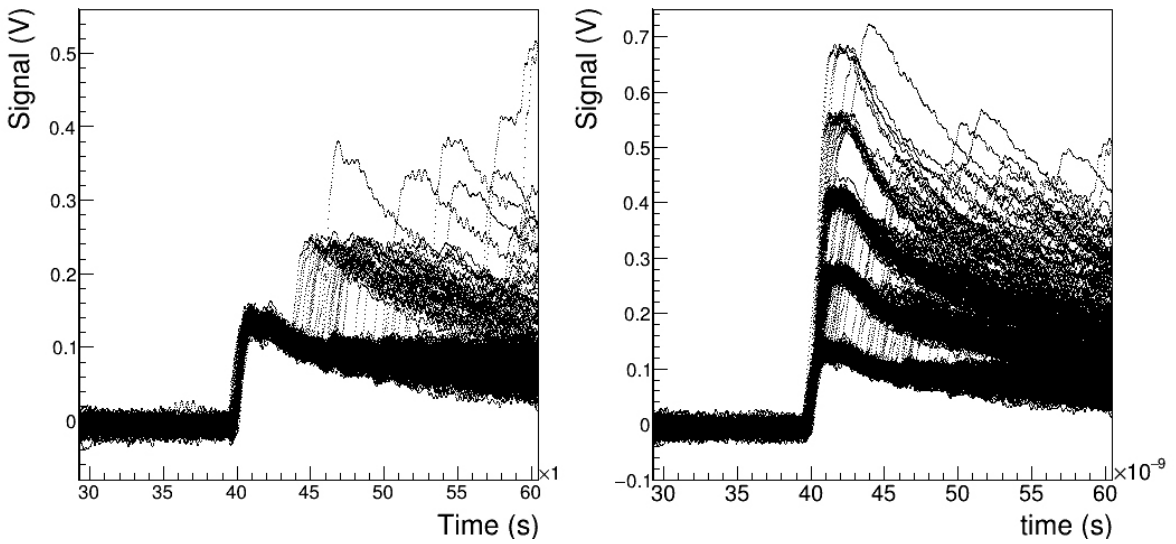

Figure 3.16: Example of signals obtained with the laser beam focused at the center of a randomly selected SPAD. Selection of the single SPAD signal (left), single+multi-SPADs signals (right). Note how correlated noise events are visible (especially in the left figure) as peaks following the primary event; not compromising the extraction of time resolution, these events were not excluded from the analysis.

The RMS used in Equation 1.23 to determine the σ_{jitter} of the electronic noise, was evaluated in the region immediately preceding the signal for each event and subsequently averaged. In Figure 3.17 (left) it is possible to see the time resolution measured as a function of the CFD for different applied voltages. Figure 3.17 (right) shows a detail of time resolution versus applied voltage for the best value of CFD (40% of the maximum amplitude) and the intrinsic resolution of the SPAD extracted using the Equation 1.25.

Time resolution as a function of sampling Bandwidth

The oscilloscope Wave-Master SDA 816Zi-A used for the measurements has a bandwidth of 16GHz. It was decided, despite the Cividec 20dB amplifier has a bandwidth of 2GHz, to take data at full bandwidth and then perform a software reduction of the bandwidth. Each i-th point of the signal was replaced with the average signal of the points in the interval [i-N, i+N]. With this method, it is possible to introduce a low-pass filter that reduces the bandwidth of the signal waveform by a factor of about 2N+1 (Figure 3.18).

It has been verified, comparing data taken directly with a bandwidth reduced to 200 MHz on the oscilloscope and data taken at full bandwidth with a successive software reduction, that the two methods are almost equivalent.

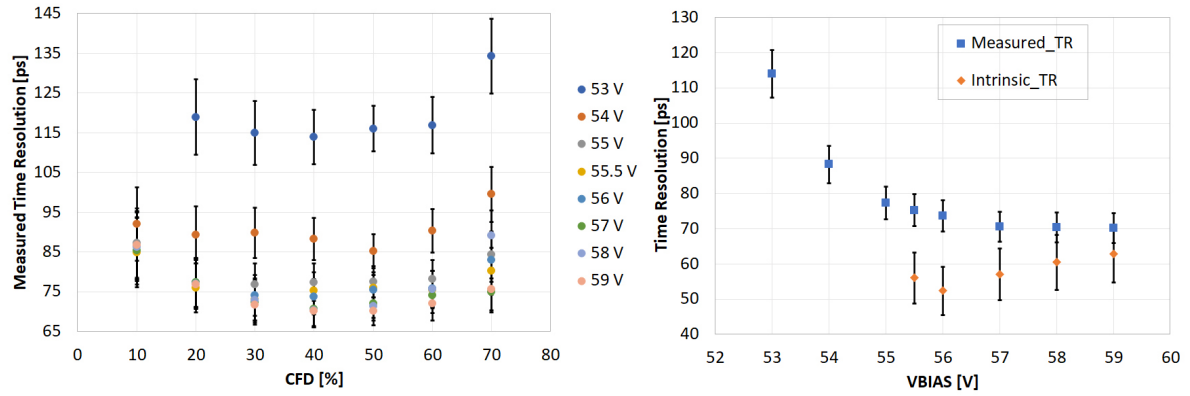

Figure 3.17: Single SPAD TR of HPK SiPM obtained with 1054 nm full power pulsed laser. TR as function of CFD for different voltages (left). TR measured and intrinsic as function of VBIAS for the 40% CFD value (right). The intrinsic resolution was evaluated only if the S/N ratio was > 10*. Only single SPAD events are included in this analysis. Laser setup.*

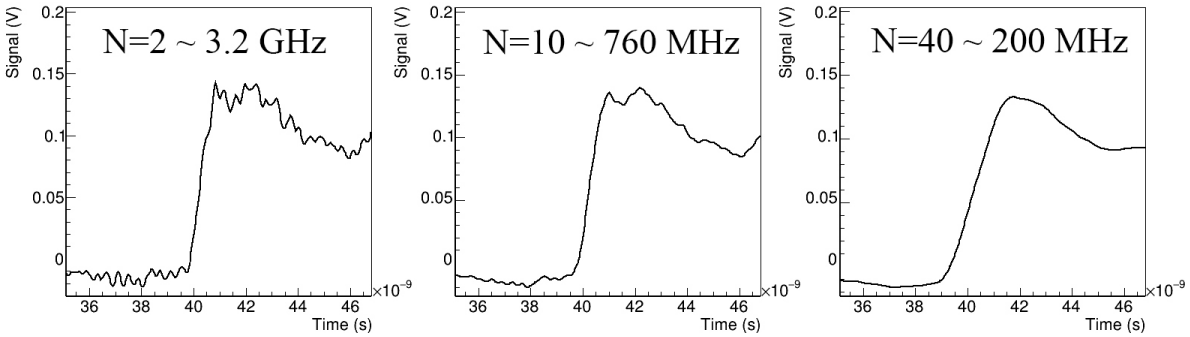

Figure 3.18: Example of signal for different values of low pass filter in the bandwidth, introduced in a software way with an average of consecutive points. The figure shows the N value used and the equivalent reduced bandwidth obtained starting from original data taken with the oscilloscope at 16 GHz.

Figure 3.19 shows the time resolution measured (left) and intrinsic (right) for different values of the Bandwidth. We did not go beyond 3.2 GHz considering the limitation of the amplifier.

The reduction of the bandwidth mainly produces two effects: the first, limiting the slope of the signal (dV/dt), increases the effect of electronic jitter which is inversely proportional to the derivative of the signal (Equation 1.23) and worsening its time performance. At the same time, excluding the higher frequencies, makes the whole measurement less subject to noise ensuring a good S/N ratio even at voltage values close to

V_{BD}. Both effects must be taken into account in choosing the optimal bandwidth to use for the timing applications of these devices.

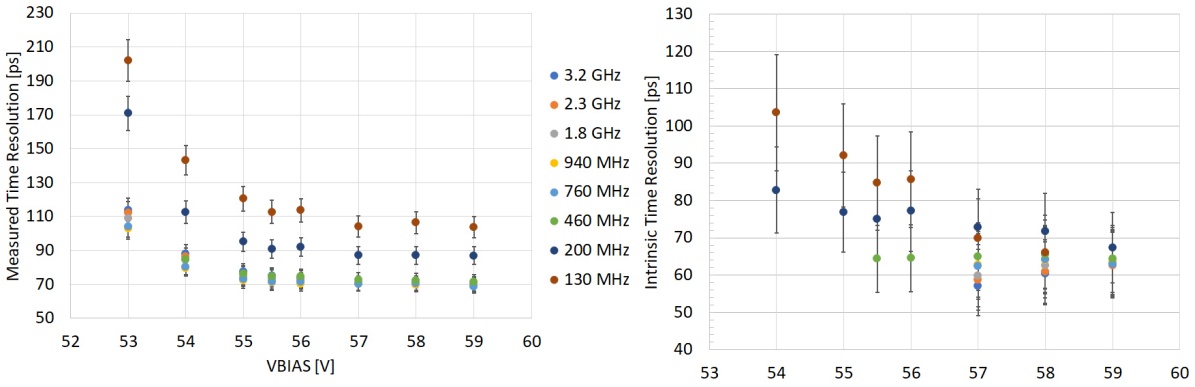

Figure 3.19: Measured (left) and intrinsic (right) TR as a function of VBIAS for different value of Bandwidth uppercut. The same data were used with a software reduction of the Bandwidth, for each VBIAS ~ 15k events were selected and the 40% CFD was selected. The intrinsic resolution was evaluated only if the S/N ratio was > 10*. Only single SPAD events are included in this analysis. Laser setup.*

It can be noted in Figure 3.19 that the measured time resolution remains almost uniform down to a bandwidth of 460MHz. Below this value, a further reduction of the bandwidth returns a worse measure of time resolution. On the other hand, the evaluation of the intrinsic TR shows that the measured intrinsic time resolution tends to assume the same value of ~65ps at high overvoltage, independently of the bandwidth chosen. The method used to evaluate the intrinsic resolution (relation1.23) overestimates, however, the contribution of the jitter when the Signal/Noise (S/N) ratio is too low (a condition particularly evident at low VBIAS if high frequencies are included) making the estimates of intrinsic time resolutions at low voltages non-physical. An interesting result of the measured intrinsic time resolution in the entire range of overvoltage shown is represented by the values taken at 200 MHz: thanks to the low S/N ratio guaranteed by the reduced bandwidth, it is possible to measure the intrinsic time resolution even at low overvoltages. In the CR setup described in Section 3.3.1 a bandwidth of 200 MHz was used.

Time resolution as a function of light intensity

Another study carried out on the single SPAD was to evaluate the time resolution as a function of the amount of light delivered by the PiLas 1054 nm laser on the SPAD. The setup has the possibility of acting with a tune that allows passing from the full-power situation to the condition of maximum attenuation. By mechanically acting on the optics of the laser head, it is also possible to reduce the amount of light entering the single-mode optical fiber, until reaching the condition of Single Photon. The time

resolution as a function of the laser tune is shown in Figure 3.20, on the left the resolution measured on the right the intrinsic one, always evaluated through the relation 1.23. All measurements were made with a VBIAS of 58V.

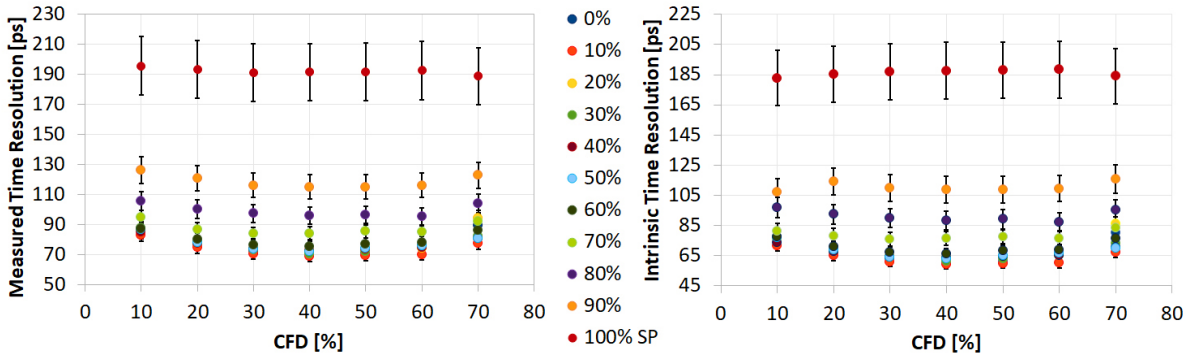

Figure 3.20: Measured (left) and intrinsic (right) TR as function of CFD for different values of tune. Tune 0% corresponds to the maximum light intensity, tune 100% is the Single photon condition. All measures done with a VBIAS of 58V. Only single SPAD events are included in this analysis. Laser setup.

It can be seen that there is a general correlation between light hitting the SPAD and time resolution: time resolution improves with 1054 nm laser light intensity. It is not exactly clear whether this relationship is due to setup limitations or is to be found in the nature of the interaction of the 1054 nm photons within the SPAD.

3.4.2 Differences between SPADs in the sensor

Each of the series of measurements shown in the previous paragraph was carried out by randomly choosing a SPAD within the HBK SiPM. In the setup with CR illustrated in the Section 3.3.1, however, the entire sensor area was exposed. Therefore, any delays in the collection of the signal in different areas of the sensor or non-uniformity between SPADs must be considered. Some studies have been performed to verify the uniformity of the response of the SPADs inside the sensor, inspired by other studies that have reported for other SiPM some interesting effects [8][31]. Taking into account these effects, the measured time resolution σ_{TOT} can be expressed as:

$$\sigma^2_{TOT} = \sigma^2_{SiPM} + \sigma^2_{TDC} = \sigma^2_{SPAD} + \sigma^2_{Jitter} + \sigma^2_{Delay} + \sigma^2_{TDC} \tag{3.4}$$

where σ_{TDC} is the constant TDC contribution (~ 7 ps using the Master SDA 816Zi-A oscilloscope) and σ_{SIPM} the time resolution of the entire SiPM. This therm includes σ_{SPAD} that is the average intrinsic time resolution of the single SPAD, σ_{Jitter} the Jitter therm due to interconnection between detector and amplifier and σ_{Delay} the contribution

due to the different signal collection time, depending on the position of the SPAD inside the sensor.

Time resolution as a function of position in the SiPM

The time resolution of single SPADs in different areas of the sensor was evaluated in order to verify the uniformity in the response of the sensor. Without changing the intensity of the light, fixing the CFD, using the same overvoltage value of 58 V, and verifying the maximum focus conditions of the laser spot in all points, the evaluation of the time resolution in various SPADs of the sensor was carried out. SPADs distributed uniformly on the sensor were deliberately chosen; intentionally involving potentially critical areas such as edges or center of the sensor, in order to maximize any discrepancy between the values. Figure 3.21 shows the result of the analysis (Orange values). It is possible to note how the measured time resolution of the single SPADs is almost uniform within the sensor. Note that the resolution here measured include: intrinsic resolution of the tested SPAD $\sigma_{SPAD-int}$, σ_{Jitter} and σ_{TDC}.

Delay in the response of the SPADs in the sensor

Focusing instead on the delay in the response of the SPADs regarding the trigger given by the laser, some differences were observed in the different areas of the sensor. Figure 3.21 shows the average value, extracted from the fitted Gaussian in the TR evaluation, that expresses the delay with which, on average, the chosen CFD threshold is exceeded (green values). A maximum difference of approximately 80 ps was observed between the selected SPADs. This, even if evaluated on a small sample of SPADs, corresponds to a σ_{Delay} of ~ 25 ps. Is then possible to consider this contribution negligible: taking, for example, a measured resolution of 90 ps (previous paragraph) adding this term we obtain a σ_{TOT} of 93 ps (within the error of the measurement carried out on the single SPAD).

3.5 Unexpected crosstalk effect

In both previously described setups (laser and CR), we observed an unexpected piece of evidence regarding the crosstalk described in Section 1.4.4. It is known that the intrinsic crosstalk increases with the overvoltage in a SiPM and the response of SPAD within a SiPM should not change if the number of photons which simultaneously hit the SPAD changes [7][8]. A binary response is in fact expected from the single SPAD depending on whether or not it is hit by one or more photons or by a MIP. Furthermore, no variation in the percentage of crosstalk was expected by changing the physical event that triggers the avalanche (remember that it works in Geiger-mode). In this section, some evidence contradicting these assumptions will be presented. Note that the geometry of the CR

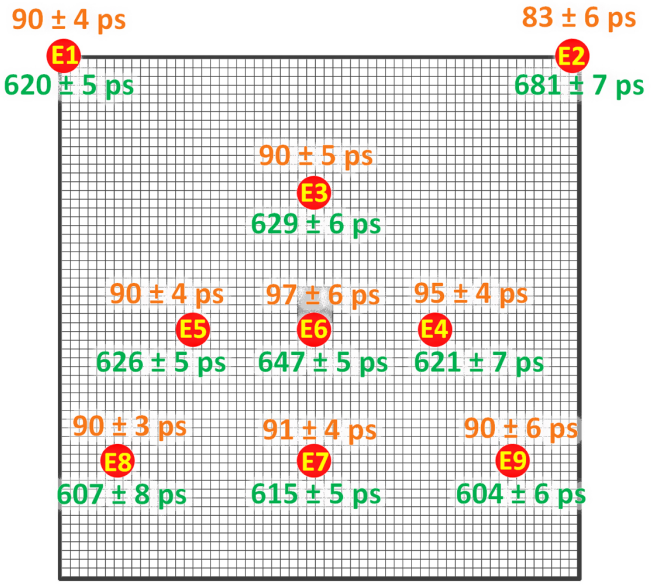

NAME	X-pos (mm)	Y-pos (mm)
E1	14.590	18.665
E2	17.540	18.805
E3	16.155	19.535
E4	15.979	20.325
E5	14.305	20.350
E6	15.839	20.370
E7	15.979	21.000
E8	14.999	21.080
E9	16.979	21.070

Figure 3.21: Measured time resolution on different SPADs of HPK SiPM (orange values) and delay, with respect to the trigger, in the response of the selected SPADs (green values). A tune of 80% of the laser light was used; 50% of CFD was selected. The red dots on the HPK SiPM drawing, represent the area where the SPAD has been selected; in the table on the right, the x-y center coordinate of the tested SPADs. Only single SPAD events are included in this analysis. Laser setup.

telescope and the coincidence of at least two SiPM makes very improbable to have inclined tracks crossing more than one SPAD.

3.5.1 Crosstalk in CR and Laser setup

The intrinsic crosstalk of the SiPM is usually evaluated by triggering on dark rate events and counting in what percentage multiple SPADs signal events occur. The CT-Fraction is defined as the ratio of multiple SPAD events and the total number of events:

$$CTFraction = \frac{\#\ multi\ SPADs\ events}{\#\ events} \tag{3.5}$$

Anomalous crosstalk was observed with both the cosmic ray setup and the laser setup (assuming a complete focus of the laser spot within the single SPAD). Figure 3.22 shows the comparison between intrinsic crosstalk (Blue), crosstalk measured in the cosmic rays

setup (Orange), crosstalk measured in the setup with laser centered on a SPAD using a 0% tune (Grey).

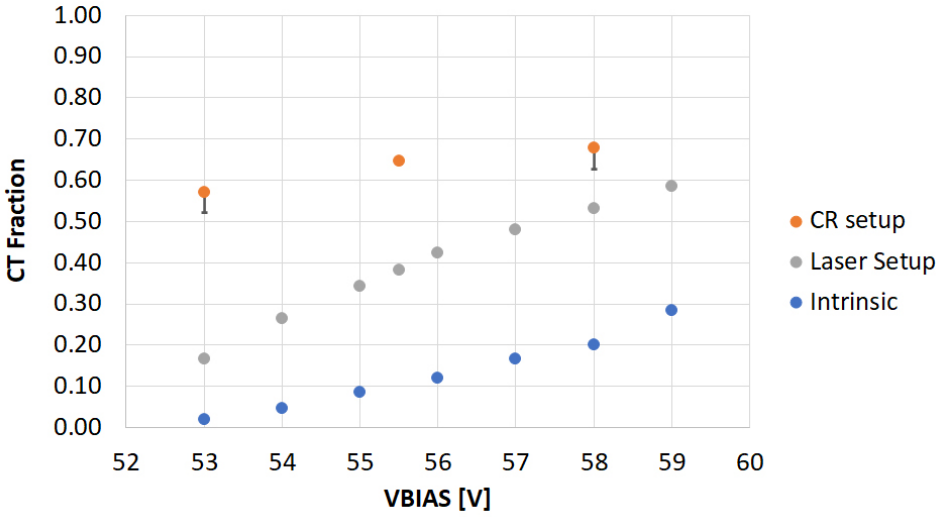

Figure 3.22: Comparison between intrinsic Crosstalk (Blue), CT measured in CR setup (Orange) and CT measured in Laser setup on a single SPAD with a 0% tune (Grey). Note that, being a count, the CT-Fraction is reported without errors. In the measurement with CR, however, having counted all the saturated events as signal events, a negative error was evaluated to take into account a possible overestimation of the crosstalk.

Figure 3.23 shows the crosstalk measured as a function of the laser tune for a VBIAS of 58V. The experimental evidence seems to suggest that crosstalk is somehow related to the number of primary pairs that a charged particle or a laser beam produces inside the silicon, and that MIPs generate a higher value with respect to photons. Note also that for almost single photons the CT fraction reached is similar to the intrinsic CT of the sensor.

However, there could be several explanations for these observations. For these reasons, we are deliberately cautious about these considerations. More insights are necessary in this context and a better understanding of the phenomenon could be obtained with a beam test of these or other SiPMs. If confirmed, this effect could be very interesting, and useful, in an application of SiPM as a detector of an ultra-fast timing layer. In fact, a greater probability of crosstalk for events generated by MIP, could help to distinguish signal events (charged particle signals) from noise events (dark count, single-photon, etc.).

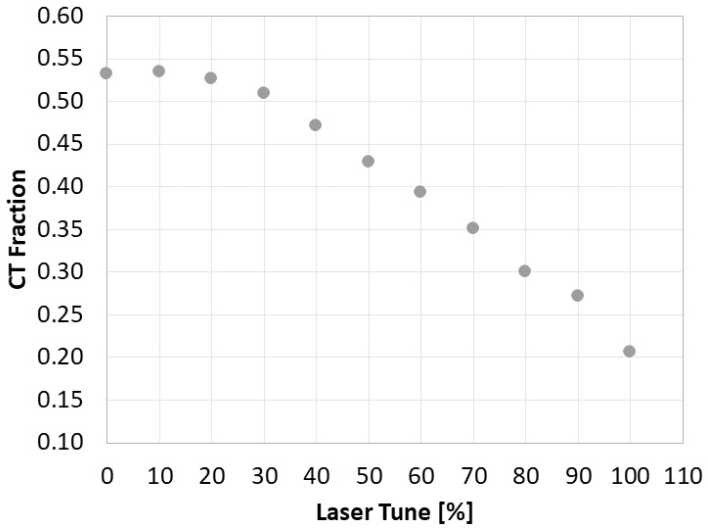

Figure 3.23: Crosstalk in the laser setup as a function of laser tune. Laser focused on the single SPAD. VBIAS of 58 V .

3.5.2 Time resolution including crosstalk events

If, on the one hand, as mentioned in the previous paragraph, a higher probability of crosstalk generated by a MIP could help in the discrimination of signal events in a HEP experiment, on the other hand, the effect is worse in terms of time resolution for the HPK SiPM. It was found that, when events with crosstalk are included in the analysis, the measured time resolution (no longer now of the single SPAD) worsens. In Figure 3.24 it is possible to see the time resolution as a function of CFD (left) for all events (single and multi-SPADs) and as a function of VBIAS for different values of CFD (right), obtained with the laser centered on a single SPAD using 0% tune. The same data used for the analysis presented in Figure 3.17 were exploited for this analysis, but this time also the events with crosstalk were included Figure 3.16 (right). Note that for each VBIAS ~15k memorized waveforms have been analyzed, the CTFraction of this dataset is shown in Figure 3.22 (grey points). It can be seen how, by inserting the crosstalk events in the laser measurements analysis, the best time resolutions are obtained for lower CFD values. Using average CFD values (such as 50%) it can be noted that as the overvoltage increases a minimum is reached and then there is a worsening of the measured time resolution, an effect less evident for low CFD values.

In the case of the CR Setup, since the crosstalk percentages were very high (Figure 3.22), it was therefore decided to use all the single and multiple SPADs events in the determination of time resolution in order to increase the statistic.

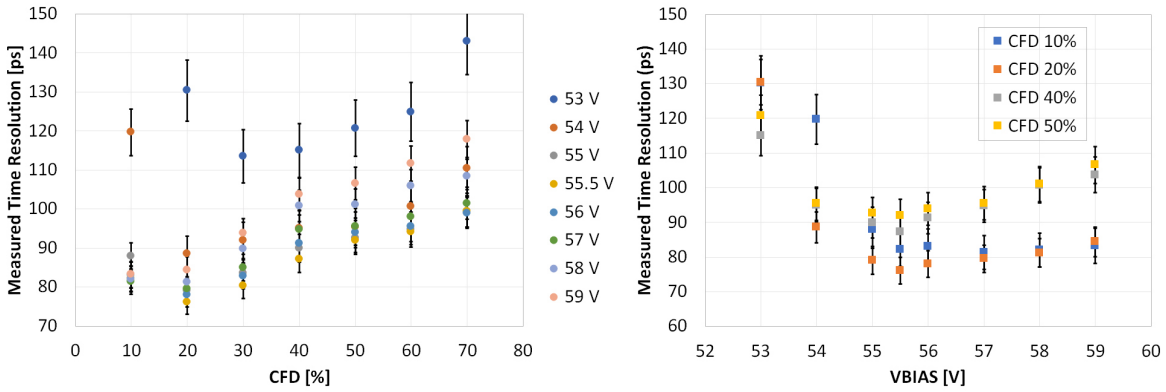

Figure 3.24: Measured TR as a function of CFD including crosstalk events (left) and as function of VBIAS (right). All events (single and multi-SPADs) are included in the analysis. Laser setup.

3.6 Comparison of cosmic rays and laser setup for HPK SiPM

As a final comparison between the cosmic rays and laser setup in Figure 3.25 the measured and extracted intrinsic time resolutions obtained with the two setups are reported together. No changes, except the primary source, have been made: the data have been taken with the same bandwidth and with the same setup always using the biasing and readout circuit shown in Figure 3.9, with the signal amplified by the Cividec 20dB amplifier. In the time resolution measurement with the laser, a 0% tune was used; crosstalk events were also considered and a term was added in order to take into account the time resolution contribute introduced by the different delay in the response in various parts of the sensor (Section 3.4.2).

The intrinsic time resolutions are perfectly compatible within the errors, even if a higher statistic is necessary to improve the measurement with charged particles. It should also be noted that these measurements were carried out with an important limitation of the bandwidth at 200 MHz, therefore they represent an upper limit in the time resolution of the HPK SiPM studied.

Focusing, for example, on the value of 55.5V as VBIAS, the SiPM HPK S13360-3050VE has proved able of reaching a time resolution of 113±27 ps in the direct detection of charged particles. The time resolution obtained with the laser setup for the same VBIAS, under the same experimental conditions and including all the contributions of the SiPM time resolution (Equation 3.4) is 95±11 ps.

It must be emphasized that the statistics in CR measurements is low moreover, the fluctuations linked to the nature of the CR and to long-term measurement make the considerations reported here preliminary and to be confirmed/corrected with the use of

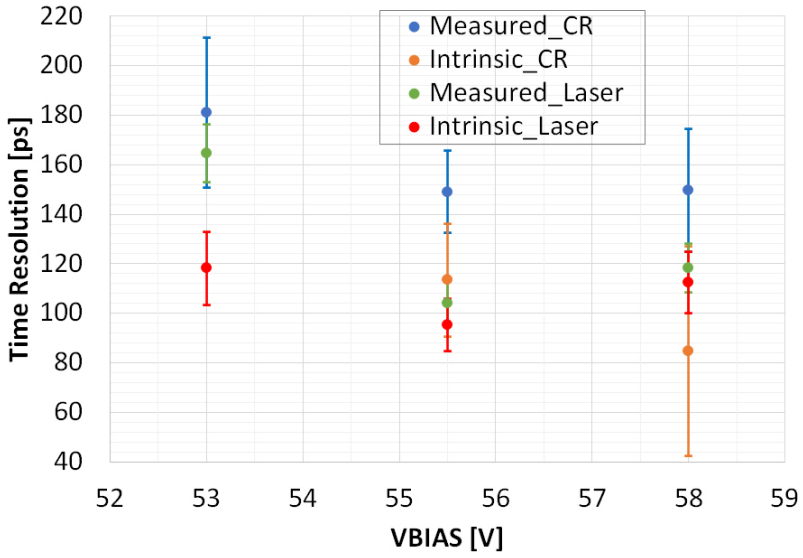

Figure 3.25: Comparison between measured and intrinsic HPK SiPM time resolution obtained with the CR and Laser setup. To better compare the results, a 0% laser tune was used in the laser measurements and crosstalk events are also considered in the analysis; a correction was also introduced that took into account the σ_{Delay} obtained (Section 3.4.2). All events (single and multi-SPADs) are included in the analysis.

the data that will be taken in Autumn 2021 at beam test.

Removing the low-pass filter in the bandwidth used in the comparison with the CR setup results, selecting the single SPAD events and using a considerable amount of focused 1054 nm light, the measurements obtained with the laser, that were much faster and easier to carry out in the laboratory, essentially confirm the intrinsic time resolution already found on the same sensor in other works. For reference, the results of studies carried out by Gundacker S. et. al [32] are reproduced in Figure 3.26, where is reported the intrinsic time resolution measured for different SiPM in single-photon conditions with laser light of 420 nm. It can be seen that SiPM similar to the one used in the present thesis, red points in the Figure 3.26, shows approximately the same time resolution of ~60ps obtained with the 1054 nm laser with low tune conditions setup Figure 3.17 (note that in this work we report the sigma while the Figure 3.26 shows the FWHM, which corresponds to 2,35 sigma). However the similar result is obtained in quite different conditions (intense 1054 nm in our case and single-photon 420 nm in [32]) and, moreover, in our setup, as described in Section 3.4.1, a progressive worsening of the time resolution decreasing the IR light intensity was observed. As mentioned, it is not clear if this is a limit of our setup or if it is due to the different interactions that IR and blue light have inside the SPAD. Future studies with a 1054 nm single photon are needed to investigate

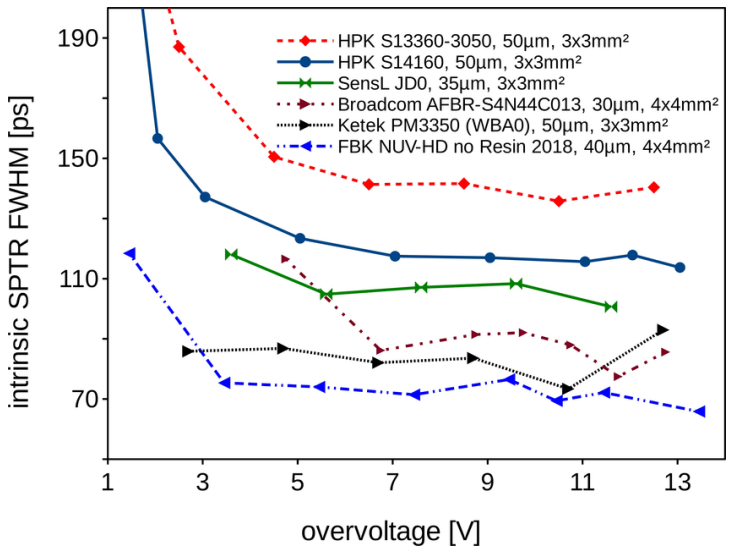

Figure 3.26: SPTR measured by Gundacker S. et. al [32] with 420nm pulsed laser on SiPM HPK S13360-3050VE and other devices.

the phenomenon.

In Figure 3.26 it can be also be noted that, when studied with single 420 nm photons, several other SiPMs have much better performance in terms of time resolution. This, combined with the result obtained in this work, where there is no significant worsening in time resolution when charged particles instead of photons are revealed with a SiPM, represents an excellent starting point for future studies in this direction, where SiPMs are used as direct detectors of charged particles.

3.7 Time resolution of FBK Silicon prototypes

As mentioned in Section 3.1, other SiPM prototypes were also tested. In a recent production, the FBK has produced SiPMs made with the "HD technology" that allows producing extremely small SPADs with a reduced Gain, allowing to reduce afterpulsing and crosstalk while still maintaining an excellent Fill-Factor [33]. The effect on the time resolution of these objects is not clear yet. Here is a brief summary of some preliminary studies on the time resolution of these prototypes. The same study technique illustrated in Section 3.4.1 was used on the three tested FBK sensors, Figure 3.1 b,c and d, whose main characteristics have been reported in Table 3.2.

The time resolution as a function of the CFD for the various VBIAS studied, obtained by selecting only single SPAD events, is shown in Figure 3.27 (left). It can be noted that in these prototypes the best time resolutions are obtained for low CFD values. Figure 3.27 (right) shows the measured and intrinsic time resolutions of the three SiPMs from

the FBK obtained using a CFD of 10% and using a 0% laser tune. Also in this case, the intrinsic time resolution was calculated only for the overvoltage values that had a signal to noise ratio > 10. In our 1054 nm laser setup, these detectors seem to be able to reach intrinsic resolutions of the order of 50ps, therefore they are slightly more performing than the SiPMs from HPK described in the previous sections.

The same analysis was repeated considering also the multi SPADs events in a similar way as done in the Section 3.5.2. However, in this case, the size of the SPADs, especially in the prototypes at $15\mu m$, is comparable with the size of the laser spot (estimated of the order of 10 μm), thus it cannot be said with a good level of confidence that these are all crosstalk events (due to setup limitations as vibration or photons in the Gaussian tails of the laser spot). The results of this analysis are shown in Figure 3.28.

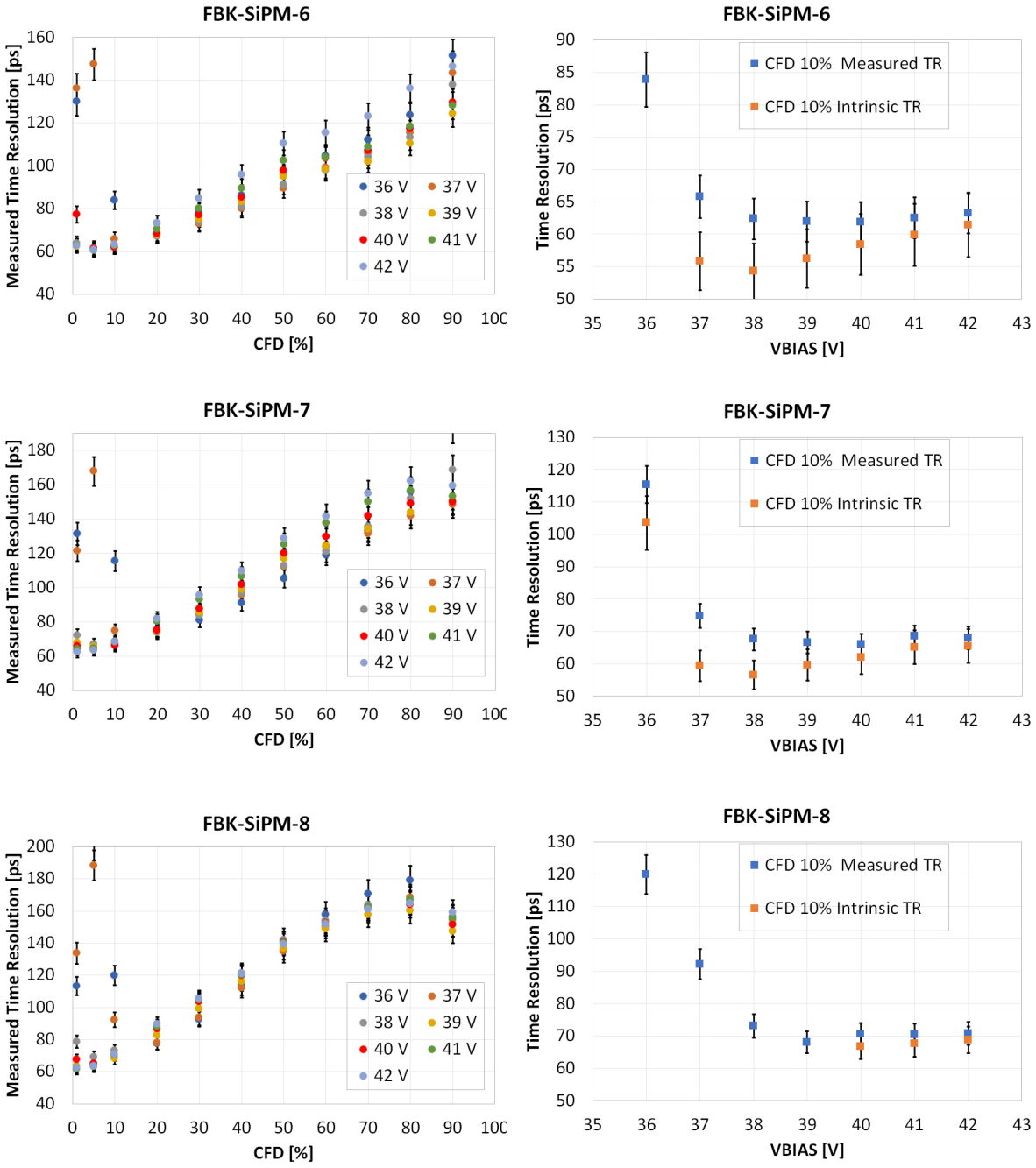

Figure 3.27: Single SPAD TR of FBK SiPMs obtained with 1054nm full power pulsed laser. TR as function a of CFD for different VBIAS(left). TR measured and intrinsic as function of VBIAS for the 10% CFD value (right). The intrinsic resolution was evaluated only if the S/N ratio was > 10. *Only single SPAD events are included in the analysis. Laser setup.*

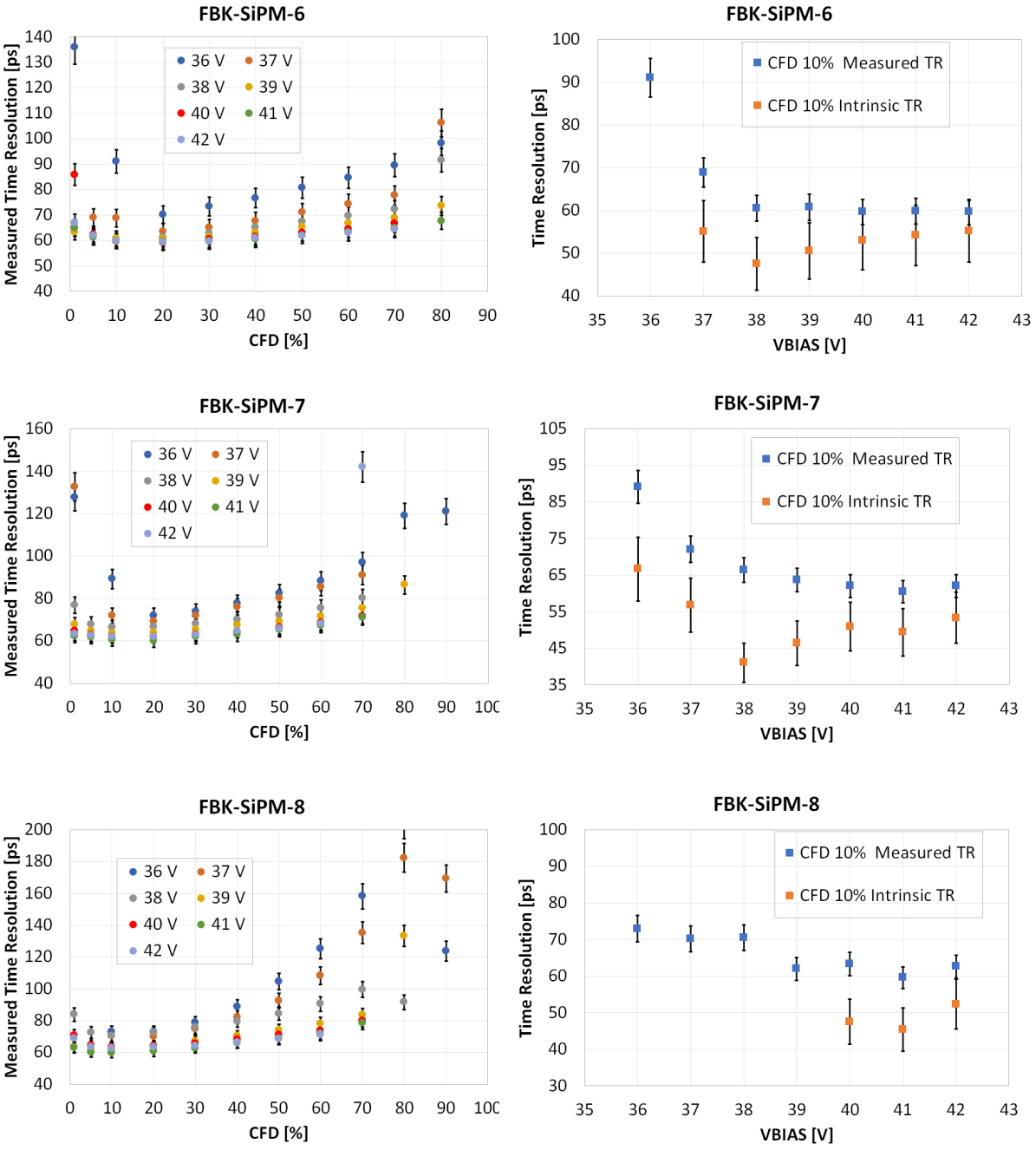

Figure 3.28: Single and multi-SPAD TR of FBK SiPMs obtained with 1054 nm full power pulsed laser. TR as a function of CFD for different VBIAS (left). TR measured and intrinsic as function of VBIAS for the 10% CFD value (right). The intrinsic resolution was evaluated only if the S/N ratio was > 10*. All events (single and multi-SPADs) are included in the analysis. Laser setup.*

3.8 Laser-measured time resolution of all tested SiPMs

in Figure 3.29 a comparison between measured (left) and intrinsic (right) time resolution obtained with all SiPMs tested using 1054 nm laser light focused in the center of a SPAD and including multi-SPAD events in the analysis. As it possible to see, the FBK SiPMs are slightly better performing in terms of time resolutions, reaching, an intrinsic resolution of about 50 *ps*. These measurements were made in conditions of full 1054 nm laser light intensity (0% tune).

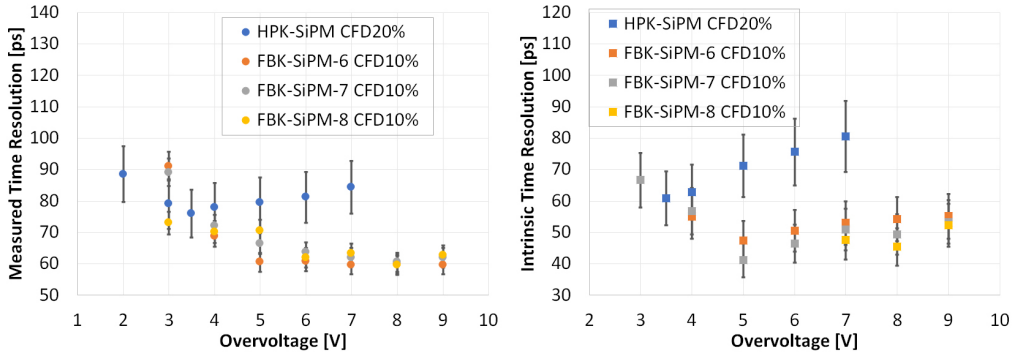

Figure 3.29: Measured (left) and intrinsic (right) time resolution as a function of VBIAS of all SiPM tested. Obtained in 1054 nm laser setup in full light intensity condition (0% tune). Also multi-SPADs events are included in this analysis. The intrinsic resolution was evaluated only if the S/N ratio was > 10*. Laser setup.*

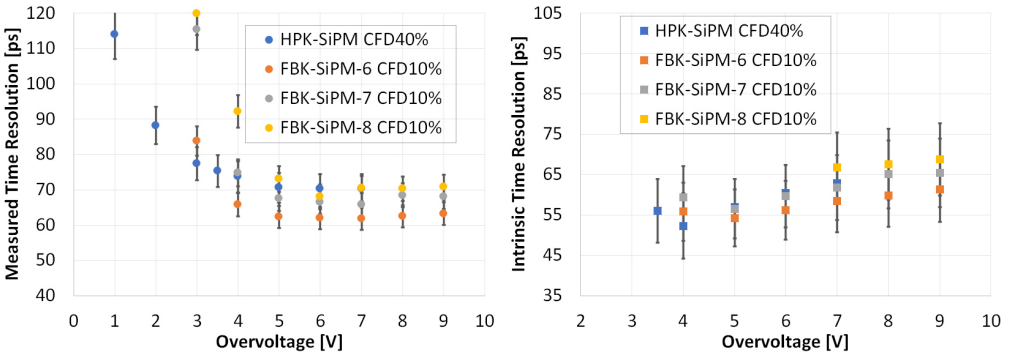

Figure 3.30: Measured (left) and intrinsic (right) time resolution as a function of VBIAS of all SiPM tested. Obtained in 1054 nm laser setup in full light intensity condition (0% tune). Only single SPAD events are included in this analysis. The intrinsic resolution was evaluated only if the S/N ratio was > 10*. Laser setup.*

A 10% CFD was chosen for the FBK SiPMs and 20% CFD for the HPK sample (these CFD values result in better time performance when crosstalk events are included as shown in Section 3.5.2). A 3.2 GHz bandwidth limitation was used for these measurements. The Figure 3.30, instead, summarizes the measured (left) and intrinsic (right) time resolution values obtained by selecting only events without crosstalk (single SPAD). Here the differences between HPK and FBK sensors are less marked. Note that in this comparison a 40% CFD was chosen for the HPK sensor as it corresponds to the best time performance of the device when only the single SPAD is selected.

Conclusions

A comprehensive study using a 1054 nm pulsed laser focused on a micrometric spot was performed on several SiPMs. After some characterization measurements, the detector's response was investigated through automatic scans performed with a LabVIEW program. By illuminating single SPADs in the tested SiPMs, all contributions affecting the time performance of the device were determined and their intrinsic time resolution was evaluated.

The results obtained with the cosmic rays setup, although to be considered preliminary, seem to suggest that the SiPM technology is well suited for the direct detection of MIPs for timing purposes. To our knowledge, this is the first evidence for such a possibility. In the test performed using the commercial device HPK S13360-3050VE an intrinsic resolution of 113±27 ps was obtained with a VBIAS of 55.5V, comparable to the time resolution obtained with a 1054 nm laser, focused on single SPADs of the SiPM which is 95±11 ps. The same experimental conditions were used for this comparison, using the same biasing and readout circuit, introducing the same low-pass filter in the oscilloscope bandwidth, and considering crosstalk events. These time resolution values are slightly worse than those obtained with single photon studies, using light in different wavelengths, found in the literature.

Values of intrinsic time resolution comparable with those reported in the analyzed references, however, were obtained with the HPK SiPM by analyzing only single SPAD events and expanding the bandwidth of the oscilloscope up to 3.2 GHz. In these conditions, an intrinsic time resolution of ~60 ps was measured.

It has been shown that by increasing the amount of 1054 nm light focused on the single SPAD there is an unexpected improvement in the time resolution of the detector. Future studies are needed to determine the cause of this effect.

Also, there is evidence that there is a considerable increase in SiPM crosstalk with charged particles or in bright light conditions, compared with the intrinsic crosstalk of the device. The results seem to suggest that the passage of a charged particle, on average, generates an avalanche of more SPADs. For this effect, further studies are also needed.

Studies on recently produced FBK prototypes also look promising in terms of time resolutions. Due to the lack of time, it was not possible to test them as charged particle

detectors, but in laser studies in low tune conditions with an oscilloscope bandwidth of 3.2GHz, an intrinsic resolution of ~50 ps was measured considering also multi-SPADs events.

During this work, many technical challenges were faced in the laboratory during the study of detectors so small and difficult to test in a laser setup with a micrometric spot. Among all, the difficulty in studying the individual SPADs (as small as $15\mu m$) made the development of a specific LabVIEW software for centering and correct focusing of the laser beam fundamental, as well as the introduction of progressive improvements to the laser setup to minimize the electromagnetic noise generated by the used instruments.

Continuous improvements have also been made to the ROOT macros used for the analysis of the data taken with the oscilloscope. Although not described here in detail, various techniques of analysis and studies on the data cuts were made in the preliminary phase of this work, in order to achieve an optimal selection of data and a comfortable level of automatism in the analysis.

The Cosmic Ray test required several months of data taking due to the small size of the detectors but, despite the poor statistics, it showed interesting and promising results. Confirmations or corrections to what is reported in this study will be provided by the next beam tests scheduled at CERN in autumn 2021 where the SiPM studied here will be tested directly with high flows of charged particles. Important tools were produced for data analysis and comparison with the most convenient measurements that can be performed with lasers in the INFN laboratories in Bologna. In this context, this work is to be considered a preparatory activity for those future studies, having identified some interesting points on which to focus the analysis.

Acknowledgements

Questo lavoro, frutto di diversi mesi di piacevole lavoro, rappresenta la conclusione di un ciclo di studi del quale ho solo ricordi positivi. Diverse le splendide persone incontrate in questo percorso che hanno contribuito in maniera diretta e non al raggiungimento di questo mio risultato. Vorrei qui citarne alcune esprimendo loro la mia più profonda gratitudine per tutto ciò che hanno fatto per me in questi anni.

Ringrazio anzitutto la mia relatrice Prof.ssa Gilda Scioli per avermi seguito, con la sua caratteristica dedizione, in questo e nel precedente lavoro di tesi triennale; e per l'apprezzatissimo supporto che, con immensa passione per il suo lavoro, offre continuamente ai suoi studenti.

Ringrazio il Dr. Rosario Nania che, con la sua stimata esperienza, mi ha sempre fornito apprezzati e utilissimi consigli nei mesi di preparazione di questo elaborato.

Ringrazio Daniele Cavazza per il suo continuo supporto in laboratorio; per avermi aiutato, grazie alla sua esperienza e alla sua creatività, a risolvere i continui problemi riscontrati nell'attività di ricerca e per aver reso piacevoli le tante ore in laboratorio.

Ringrazio tutto il gruppo ALICE della sezione INFN di Bologna, per aver contribuito in maniera determinante nello svolgimento di questo lavoro di tesi.

Particolare menzione a Francesca, un'amica oltre che Co-supervisor di questa tesi. Mi ha guidato in tutte le fasi di questo lavoro, con la sua tipica ed invidiabile dedizione, e con la sua estrema disponibilità ad ogni ora del giorno (e della notte). È inoltre stata per me un importante punto di riferimento nelle scelte personali di quest'ultimo periodo, sempre pronta dare consigli (a volte non ascoltati ☺) e supporto. La ringrazio enormemente augurandole il meglio per la sua nascente, e a mio parere molto promettente, carriera.

Ringrazio Tutti i miei amici “veterani” ormai abituati a sopportarmi: Alessandro, Andrea, Daniele, Manuel, Raffaella e Vittorio (in ordine alfabetico per evitare discussioni). Sono stati loro ad aver reso piacevoli, oltre che i miei anni passati, i periodi di tregua fra una sessione e l’altra. Troppe le esperienze vissute insieme (e troppo imbarazzanti alcune) per essere qui citate, ma per sempre impresse nella mia memoria i giorni passati con voi. Anche se lontani negli ultimi anni siete e sarete sempre un pezzo del mio cuore.

Grazie anche a tutti gli altri “amici di giù”. Siete troppi in numero per essere qui citati tutti, ma non meno importanti.

Ringrazio tutti gli amici “Bolognesi”, conosciuti a Bologna ma provenienti da ogni parte dell’Italia e del mondo.

Gli “amici di Fisica” con i quali ho condiviso le ansie di questi anni e le lunghissime ore di lezione, oltre che indimenticabili serate. Particolare il ringraziamento a Laura e Luigi, per le piacevolissime esperienze vissute con voi in questi anni.

Gli “amici di Studentato” conosciuti in questi anni fra una residenza e l’altra: Andi, Anita, Antonio, Arzana, Aura, Carlotta, Chi-hsiang, Davide, Enrico, Fatima, Frances, Francesco, Giorgia, Giulia, Ilaria, Isabella, Luca, Lucia, Mariagrazia, Michele, Milad, Natalia, Nello, Paraham, Roberta, Sarah, Serena, Uzair, Valeria, e tutti quelli che qui non ho dimenticato di citare ma che non sono meno importanti. Grazie per essere stati la mia grande famiglia in questi anni, grazie per aver reso piacevoli i miei pomeriggi e condiviso con me le vostre e le mie esperienze da fuori-sede. Grazie per avermi reso partecipe delle cene multietniche e delle innumerevoli, a volte ingiustificate, feste di studentato (con gli inevitabili kg di sovrappeso indotti).
Grazie anche ad E.R.G.O. e a tutto il suo personale, per aver reso possibile tutto ciò grazie al suo indispensabile supporto economico, senza il quale questi anni di studio sarebbero stati molto più complicati.

Un Ringraziamento particolare ai carissimi Beppe, Mattia e Samule. Compagni di viaggio della maggior parte di questo percorso. Più di altri complici delle innumerevoli avventure degli ultimi anni. Grazie per avermi regalato una esperienza di profonda e sicuramente duratura amicizia (non dimenticatevi del nostro appuntamento l’8-08-2028!!)

Un grande grazie alla mia Famiglia, mia madre, mio padre, mio fratello e mia sorella. Grazie per il vostro continuo supporto incondizionato. Sono profondamente debitore con tutti voi di quello che mi avete dato e continuate a darmi ancora, ho una profonda stima

di voi e vi ringrazio enormemente per ciò che fate per me.

Grazie a Marika, la mia ancora negli ultimi 4 anni. Grazie per aver tollerato con me questa complicata relazione a distanza, separati da centinaia di km per lunghissimi e insopportabili periodi. Grazie per avermi regalato tutti i nostri bellissimi momenti insieme e grazie per avermi reso felice. Spero che d'ora in poi le cose siano più facili per noi e che la nostra lunga strada da percorrere insieme sia meno intricata.

Grazie, infine, a tutti coloro che hanno contribuito alla mia formazione e alla mia educazione. Grazie ai miei insegnanti di ogni ordine e grado e grazie a tutte le straordinarie persone che hanno fatto di me quello che sono.

Appendix: Instrumentation

- Power supply: TDK-Lambda Z100-2
  - Output Voltage: 0-100 VDC
  - Output Current: 0-2 A
  - Output Power: 200 W
- Picoammeter: Keithley 6487
  - Current Ranges: 2nA - 20mA
  - Voltage Burden: 200 μV (1 mV on 20 mA range)
  - Reading Rate: Up to 1000/s
  - Best V Source Resolution: 0.2 mV
- Micrometer Positioning Stages (MPS): Standa 8MT167-25LS
  - Travel range: 25mm
  - Resolution full step: 1.25 μm
  - Resolution 1/8 step: 0.156 μm
  - Repeatability: 1 μm
  - Maximum speed: 6 mm/s
- Laser: PiLas PiL036XSM head + EIG2000DX controller
  - Control Unit EIG2000DX
    - Internal trigger Repetition Rate: 100 Hz to 125 MHz
    - Internal trigger Frequency resolution: <0.1 ppb
    - Trigger Output Amplitude: +2.5V @ 50 Ω
    - Trigger Pulse width: > 3.5ns
  - PiL036XSM head

    * Wavelength: 1057.1 nm (measured at 1MHz)
    * Spectral width: 8.9 nm
    * Fiber Connector: FC/APC
    * Output Signal FWHM: 36.7 ps (Frequency 100kHz Tune 50%)
    * Av. Power after SM fiber: 1.989 μW (Frequency 100kHz Tune 50%)
    * Energy after SM fiber: 20 pJ (Frequency 100kHz Tune 50%)
    * Peak power after SM fiber: 460 mW (Frequency 100kHz Tune 50%)

- Single Mode Optical Fiber: Torlabs P3-980A-FC-1
  - Operating Wavelength: 980 - 1550 nm
  - Cutoff Wavelength: 870 - 970 nm
  - Mode Field Diameter: 5.3-6.4 μm @ 980nm
  - Cladding Diameter: 125 μm
  - Length: 1 m
- Fiber Collimator: Schäfter+Kirchhof 60FC-T-4-M40-54
  - Focal length: 40 mm
  - AR coating: 54
  - Wavelength range: 630 - 1080 nm
  - Clear aperture: 17 mm
  - Connector type: FC/APC
- Micro Focus Optics: Schäfter+Kirchhof 13M-M40-54-S
  - Focal length: 40 mm
  - AR coating: 54
  - Wavelength range: 630 - 1080 nm
  - Clear aperture: 15 mm
- Main Oscilloscope: Teledyne LeCroy Master SDA 816Zi-A
  - Analog Bandwidth @ 50 Ω (-3dB): 16 GHz (>10 mV/div)
  - Rise Time (20-80% @ 50 Ω): 21.5 ps
  - Bandwidth Limiters: 20 MHz, 200 MHz, 1 GHz, 4 GHz, 6 GHz, 8 GHz, 13 GHz
  - Maximum imput Voltage (@ 50 Ω): ±5V

  - Time/Division Range: 20 ps/div - 128 s/div
  - Clock Accuracy < 1 ppm + (aging of 0.5 ppm/yr from last calibration)
  - Trigger and interpolator jitter: < 0.1 ps_{rms} (typical, software assisted), 2 ps_{rms} (typical, hardware)
  - Single-Shot Sample Rate/Ch: 40 GS/s on 4 Ch
  - Clock Recovery Jitter: 2 ps rms + 0.3% Unit Interval rms for PRBS data patterns with 50% transition density (typical)

- Main Amplifier: Cividec C2-HV Broadband Amplifier
  - Type: Current amplifier
  - Analog bandwidth: 1 MHz - 2 GHz
  - Gain: 40 dB
  - input coupling: AC coupled (1 nF @ 1 kV)
  - input impedence: 50 Ω
  - Linear output voltage range: ±1 V
  - Output impedance: 50 Ω
  - Equivalent input current noise (rms): 0.4 μA

References

[1] Fabjan C.W. and Herwig S. *Particle Physics Reference Library, Volume 2: Detectors for Particles and Radiation.* Springer, Gewerbestrasse 11, 6330 Cham, Switzerland, 2020.

[2] Väyrynen S. Irradiation of silicon particle detectors with mev-protons. *ACADEMIC DISSERTATION UNIVERSITY OF HELSINKI*, 2010.

[3] P.A. Zyla et al. *Particle Data Group.* 2020.

[4] Boit C. et al. From ic debug to hardware security risk: The power of backside access and optical interaction. *Conference Paper*, 2016.

[5] Carnesecchi F. *Experimental study of the time resolution for particle detectors based on MRPC, SiPM and UFSD technologies.* Università di Bologna, PhD in Fisica, XXX ciclo, 2018.

[6] Hartmut F-W S. et al. 4d tracking with ultra-fast silicon detectors. *Rep. Prog. Phys.*, 81(026101), 2018.

[7] Gundacker S. and Heering A. The silicon photomultiplier: fundamentals and applications of a modern solid-state photon detector. *Phys. Med. Biol.*, 65(17TR01), 2020.

[8] Gundacker S. Acerbi F. Understanding and simulating sipms. *Nuc. Inst. and Meth. in Physics Research, Section A*, 926:16–35, 2019.

[9] Otte A.N. On the efficiency of photon emission during electrical breakdown in silicon. *Nuc. Inst. and Meth. in Physics Research, Section A*, 610:105–109, 2009.

[10] Riccardo del Burgo, Florencia Canelli, Salvador Hidalgo, Benjamin Kilminster, Giulio Pellegrini, Anna Macchiolo, and Ivan Villa Alvarez. Gain and time resolution of thin Low Gain Avalanche Detectors. *PoS*, LHCP2019:024, 2019.

[11] Klempt W. Review of particle identification by time of flight techniques. *Nuc. Inst. and Meth. in Physics Research, Section A*, 433:542–553, 1999.

[12] Schmidt B. The high-luminosity upgrade of the lhc: Physics and technology challenges for the accelerator and the experiments. *J. Phys.: Conf. Ser.*, 706 022002, 2016.

[13] CMS Collaboration. The cms experiment at the cern lhc. *JINST*, 3 S08004, 2008.

[14] ATLAS Collaboration. The atlas experiment at the cern large hadron collider. *JINST*, 3 S08003, 2008.

[15] Apollinari G. et al. *High-Luminosity Large Hadron Collider (HL-LHC):Preliminary Design Report*. Geneva : CERN, 2015.

[16] Ruotsalainen U. Soudabeh moradi front-end data processing of new positron emission tomography demonstrator. 2014.

[17] Lecoq P. and Gundacker S. Sipm applications in positron emission tomography: toward ultimate pet time-of-flight resolution. *Eur. Phys. J. Plus*, 136(292), 2021.

[18] ALICE Collaboration. The alice experiment at the cern lhc. *JINST*, 3 S08002, 2008.

[19] Adamová D. et al. A next-generation lhc heavy-ion experiment. Geneva, Switzerland, 2019.

[20] Alice 3 workshop june 2021. `https://alice-conferences.web.cern.ch/node/63329`.

[21] A. Collaboration. Expression of interest for an alice its upgrade in ls3. *NALICE-PUBLIC-2018-013*, 2018.

[22] Turchetta R. et al. Cmos monolithic active pixel sensors (maps): New 'eyes' for science. *Nuc. Inst. and Meth. in Physics Research, Section A*, 560:139–142, 2006.

[23] Hamamatsu. Mppc for precision measurement s13360-3050ve. `https://www.hamamatsu.com/eu/en/product/type/S13360-3050VE/index.html`.

[24] Rick Bitter, Taqi Mohiuddin, and Matt Nawrocki. *LabVIEW: Advanced programming techniques*. Crc Press, 2006.

[25] Vignola G. *Realizzazione di un sistema automatico di test per rivelatori al silicio e studio preliminare di una matrice 2x2 con UFSD*. Università di Bologna, Laurea in Fisica, 2018.

[26] Simon F. Silicon photomultipliers in particle and nuclear physics. *Nuc. Inst. and Meth. in Physics Research, Section A*, 926:85–100, 2019.

[27] Sipm asd-nuv3s-p. https://advansid.com/attachment/get/up_53_1432731710.pdf.

[28] plastic scintillator bc-420. https://www.crystals.saint-gobain.com/products/bc-418-bc-420-bc-422-bc-422q.

[29] Zugec P. et al. Pulse processing routines for neutron time-of-flight data. *Nuc. Inst. and Meth. in Physics Research, Section A*, 813:134–144, 2016.

[30] McDonald W.J. Gedcke D.A. Design of the constant fraction of pulse height trigger for optimum time resolution. *Nuc. Inst. and Meth.*, 58:253–260, 1968.

[31] Nemallapudi M.V. et al. Single photon time resolution of state of the art sipms. *JINST.*, 11 P10016, 2016.

[32] Gundacker S. et al. Experimental time resolution limits of modern sipms and tof-pet detectors exploring different scintillators and cherenkov emission. *Phys. Med. Biol.*, 65 025001, 2020.

[33] Fabio Acerbi et al. Time resolution of the new sipm technologies: performance and measurements techniques. https://indico.cern.ch/event/591739/contributions/2392481/attachments/1398267/2132479/Talk_sp1-4.pdf.